Chapter 5
Testing of Carbon Fibers and Their Composites

Soo-Jin Park and Kyong-Min Bae

Abstract In this chapter, we will introduce an evaluation of carbon fibers and their composites with various analyses. The major types of methods of characterization techniques that work best for carbon fibers and their composite materials to understand their properties such as chemical, physical, and mechanical properties and advanced characterization methods for surface or morphology analyses, such as transmission electron microscopy, scanning probe microscopy, and atomic force microscopy will be described. In addition, a concise summary of all the major characterization methodologies used on composite materials will be presented.

5.1 Introduction

Composite materials have made their way into every aspect of the modern technological society, particularly in applications requiring high strength and low weight, specifically in the aerospace industry. Because composites are hybrid heterogeneous materials, they can be difficult to characterize by a single methodology. In this chapter, (1) the major types of methods of characterization techniques that work best for composite materials to understand their properties such as chemical, physical, and mechanical properties, and (2) advanced characterization methods for surface or morphology analyses, such as transmission electron microscopy, scanning probe microscopy, and atomic force microscopy will be described. Finally, a concise summary of all the major characterization methodologies used on composite materials will be presented.

S.-J. Park (✉) · K.-M. Bae
Department of Chemistry, Inha University, 100 Inharo, Incheon, Republic of Korea
e-mail: sjpark@inha.ac.kr

© Springer Science+Business Media Dordrecht 2015

S.-J. Park, *Carbon Fibers*, Springer Series in Materials Science 210,
DOI 10.1007/978-94-017-9478-7_5

5.2 Evaluation of Carbon Fibers

5.2.1 Introduction

In this section, we describe the techniques and methods that are generally used to characterize the properties of carbon fibers for application in composite materials. Sophisticated experimental techniques are required for fiber characterization and test laboratories must be well equipped for measuring the fiber properties. It is also recognized that in many cases, the measurement of a fiber property that manifests itself in the reinforced composite can best be accomplished by measuring the properties of the composites.

5.2.2 Elemental Analysis

In elemental analysis, a sample of some material (e.g., soil, waste or drinking water, bodily fluids, minerals, and chemical compounds) is analyzed for its elemental and, occasionally, the isotopic composition. A variety of quantitative wet gravimetric and spectroscopic chemical analysis techniques may be applied to analyze the compositions of and the presence of trace elements in fibers [1–4].

A suitable standardized method for carbon and hydrogen analysis, modified to handle carbon and polymeric fibers, is provided by the ASTM test method D3178 [5]. Carbon and hydrogen concentrations are determined by burning a preweighed quantity of the sample in a closed system and fixing the products of combustion in an absorption train after complete oxidation and purification from interfering substances.

Carbon and hydrogen concentrations are expressed as percentages of the total dry weight of the fiber. The ASTM test method D3174 [6] describes a related test in which metallic impurities may be determined by the analysis of the ash residue.

Li et al. [2] investigated the feasibility of activating vapor-grown carbon fibers (VGCFs) with supercritical fluids (SCFs). The quantitative analysis of the VGCFs by elemental analysis is shown in Table 5.1. The original VGCF (VGCF0) contains highly pure carbon-containing material, which consists of 97.3 % carbon, 0.08 % hydrogen, and 0.22 % nitrogen by weight. All the treated VGCFs showed the absence of any significant changes in terms of hydrogen and nitrogen; however, in VGCF3, 4, and 5, other elements such as oxygen or contaminants from the corrosion of the reactor were present in significant amounts.

Table 5.1 Elemental analysis of VGCFs [2]

Element	VGCF0	VGCF1	VGCF2	VGCF3	VGCF4	VGCF5
C (%)	97.32	97.61	97.53	64.78	71.46	92.59
H (%)	0.08	0.01	0.01	0.26	0.70	0.01
N (%)	0.22	0.18	0.15	0.23	0.15	0.09
Others (%)	2.38	2.20	2.31	34.73	27.69	7.31

5.2.3 X-ray Photoelectron Spectroscopy

X-ray photoelectron spectroscopy (XPS), also known as electron spectroscopy for chemical analysis (ESCA), is the most widely contemporary surface characterization method [7, 8]. Large amount of information can be acquired from each spectrum (Table 5.2), and the technique is flexible enough to be used on a large variety of sample types.

Each atom on the surface of a material (except for hydrogen) consists of valence electrons, which are involved in chemical bonding, in addition to core electrons. These core electrons possess a unique binding energy, which is characteristic of the type of atom to which it is bound. By analyzing the binding energies of the electrons and the peak areas, quantitative elemental surface analysis is possible [2].

Because the electrons can only travel a short distance through the sample without undergoing inelastic collisions resulting in a drastic loss of energy, XPS is considered to be highly surface sensitive. Usually, only 50–100 Å of the sample surface is analyzed using this technique [2, 8].

Surface analysis by XPS begins by placing the sample in an ultrahigh vacuum environment ($\sim 10^{-10}$ Torr) and then irradiating the material with a source of low-energy X-rays. If the frequency of the excitation X-rays are greater than the binding energy of each element, photoemission will occur. Schematics of the processes, which occur during XPS are shown in Figs. 5.1 and 5.2 [7, 8].

The resulting photoelectrons are emitted from the surface with kinetic energy (E_k) measured by a hemispheric analyzer. Using the incident X-ray energy (hv), the binding energy (E_b) is calculated using Einstein's relationship given in (5.1) [3, 7, 8], where ϕ is the work function of the spectrometer.

$$E_b = hv - E_k - \phi \tag{5.1}$$

The photoelectrons are then separated according to their energy, counted, and related to the atomic and molecular environment from which they were ejected. A spectrum of the number of emitted electrons versus binding energy is obtained.

Table 5.2 Information obtained by XPS from Ratner and Castner [7]

In the outermost 10 nm of a surface, XPS can provide
Identification of all elements (except H and He) present at concentrations greater than 0.1 at.%
Semiquantitative determination of the approximate elemental surface composition (with an error < ±10 %)
Information about the molecular environment (such as oxidation state and bonding atoms)
Information about aromatic or unsaturated structures from shake-up ($p^{*\circledR}$ p) transitions
Identification of organic groups using derivatization reactions
Nondestructive elemental depth profiles 10 nm into the sample and surface heterogeneity assessment using (1) angular-dependent XPS studies and (2) photoelectrons with differing escape depths
Destructive elemental depth profiles several hundred nanometers into the sample using ion etching (for organics)

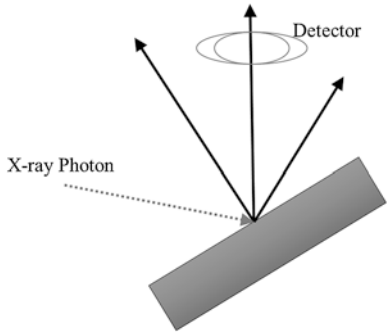

Fig. 5.1 Schematic representing processes occurring during XPS

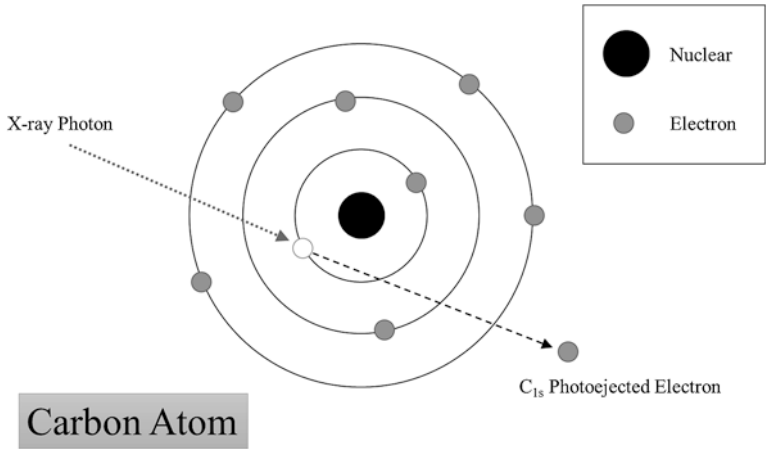

Fig. 5.2 Schematic of a carbon atom undergoing photoelectron emission [3]

Specific electrons of an atom have certain binding energies; however, the chemical environment of the atom can create variations in the values. These changes in the energy values, or chemical shifts, represent the presence of covalent or ionic bonds between atoms and help deduce the chemical structure of the material surface. Some common binding energy peak assignments for the carbon 1s peak and the oxygen 1s peak are seen in Tables 5.3 and 5.4 [3, 7, 8].

Various researchers have explored curve fitting approaches with a vast majority of the studies concentrating on core spectrum studies. Over 250 papers have addressed the curve fitting area and hence, only a brief description of the type of information that can be obtained by XPS will be presented here. A complete review of the curve fitting approach can be found in papers referenced by Sherwood [1].

Wang and Sherwood [9] showed that XPS can be used to reveal the interfacial chemistry in the carbon fiber matrix system. The use of propionaldehyde under

Table 5.3 Common binding energy assignments for carbon 1s peak from Ratner and Castner [3]

Functional group		Binding energy (eV)
Hydrocarbon	C–H, C–C	285.0
Amine	C–N	286.0
Alcohol, Ether	C–O–H, C–O–C	286.5
Carbonyl	C=O	288.0
Amide	N–C=O	288.2
Acid, Ester	O–C=O	289.0
Urea	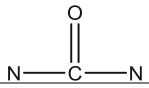	289.2
Carbamate	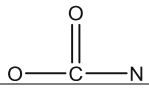	289.9
Carnonate	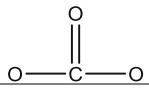	290.3

Table 5.4 Common binding energy assignments for oxygen 1 s peak from Ratner and Castner [3]

Functional group		Binding energy (eV)
Carbonyl	C=O, O–C=O	532.2
Alcohol, Ether	C–O–H, C–O–C	532.8
Ester	C–O–C=O	533.7

acidic conditions as a coupling agent is seen to yield an interfacial chemical reaction that can be interpreted to correspond to acetal cross-linking. The core and valence band XPS data can be interpreted by ab initio Hartree-Fock calculations. Air oxidation monitored by thermogravimetric analysis shows that the cross-linked samples exhibit enhanced oxidation resistance.

In Fig. 5.3, the XPS profile of the C_{1s} region of a carbon fiber electrochemically oxidized in phosphoric acid and subsequently treated with acidified PAL is presented. The separations between the component peaks are compared with the separations calculated from an ab initio calculation [9].

Previous work by researchers on the highly resolved core carbon 1s spectrum of untreated carbon fibers showed the different bonds of carbon, where the main component peak (the lowest binding energy peak) corresponded to the carbon fiber and C=C bonds. Other carbon bonds were identified by higher binding energy features corresponding to oxidation, i.e., alcohol (C–OH), carbonyl (C=O), and carboxyl (COO) and to amino C–N (Fig. 5.4).

5.2.4 X-ray Diffraction

X-ray diffraction (XRD) is a versatile nondestructive technique, which reveals detailed information about the chemical composition and crystallographic structure

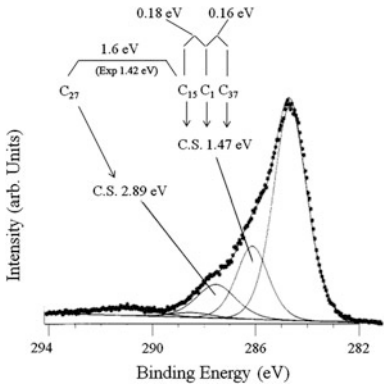

Fig. 5.3 XPS profile of C_{1s} region of a carbon fiber electrochemically oxidized in phosphoric acid [9]

of natural and manufactured materials. A crystal lattice is a regular three-dimensional distribution (e.g., cubic and rhombic) of atoms in space. The lattices are arranged such that they form a series of parallel planes separated from one another by distance d, which varies with the nature of the material. For any crystal, planes exist in a number of different orientations, each with its own specific d-spacing.

By varying the angle theta, the Bragg's Law conditions are satisfied by different d-spacings in polycrystalline materials. Plotting the angular positions and intensities of the resultant diffracted peaks of radiation produces a pattern, which is characteristic of the sample. When a mixture of different phases is present, the resultant diffractogram is formed by the addition of the individual patterns.

Using the principles of XRD, a wealth of structural, physical, and chemical information about the material investigated can be obtained. A host of XRD techniques is available for various classes of materials, each revealing its own specific details of the sample studied.

Iwashita et al. [10] investigated the application of a standard procedure of XRD measurements on carbon materials. The various peaks include the one near 29° corresponding to the 002 reflection, near 57° corresponding to the 004 reflection, the one near 75° corresponding to the 110 reflection, and the one near 89° corresponding to the 112 reflection, as shown in Fig. 5.5, respectively.

5.2.5 Raman Spectroscopy

Raman spectroscopy is a laser-based method using inelastically scattered light to investigate the vibrational, rotational, and other low-frequency modes of interaction between molecules. Raman bands are sharp peaks in the spectra that can be associated with vibration modes at the molecular level. Early studies on graphitic materials revealed that a Raman band at $\sim$1,585 cm^{-1} can be related to C–C vibrations in graphite and is present in all carbon fibers. Another band in

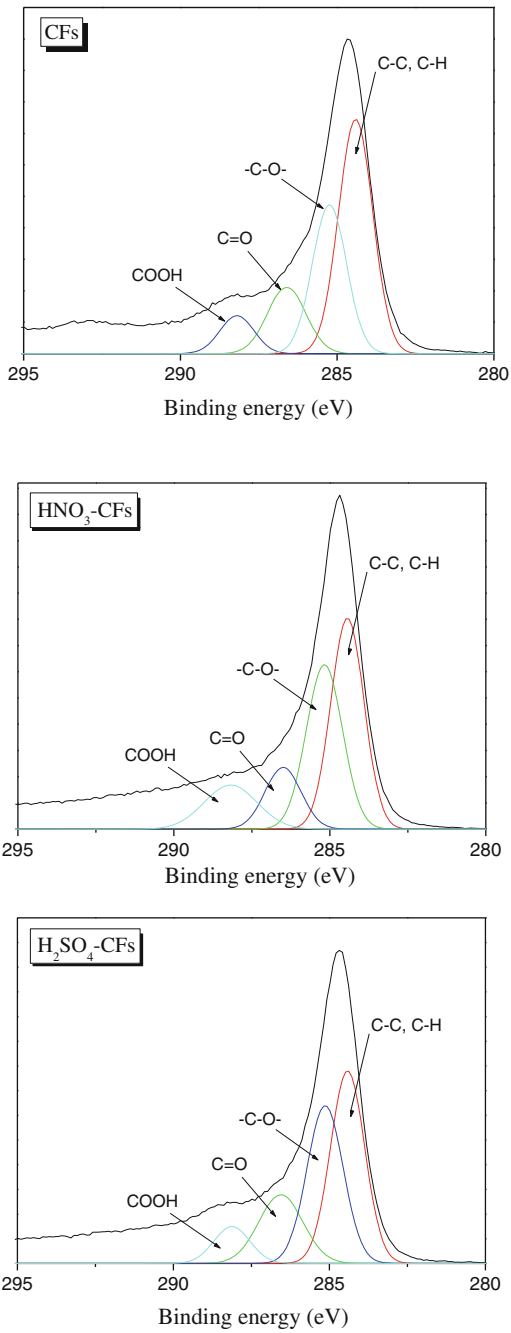

Fig. 5.4 High-resolution carbon 1s peak of untreated carbon fibers

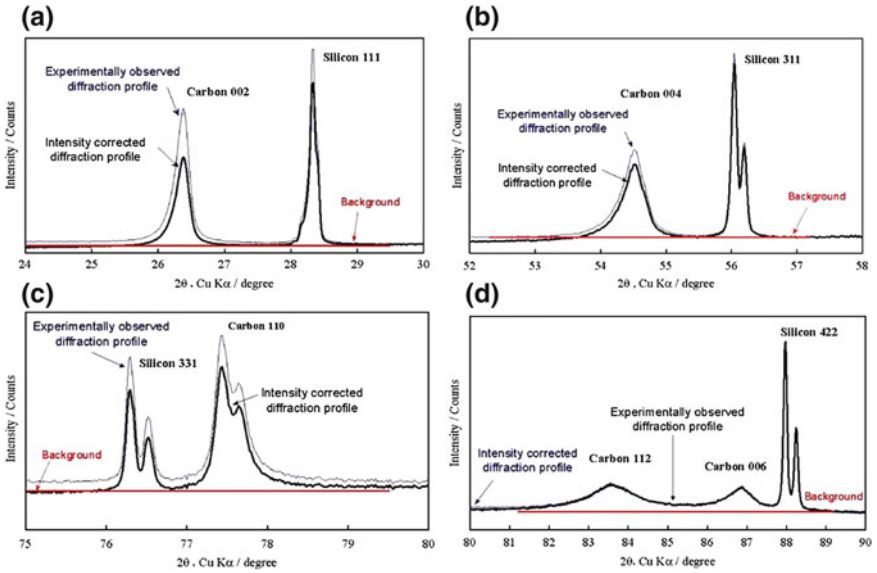

Fig. 5.5 XRD patterns of carbon materials [10]

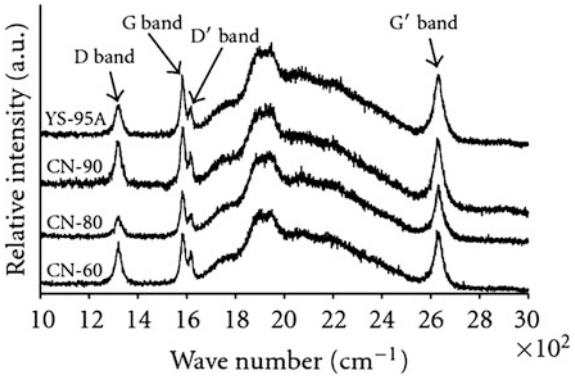

Fig. 5.6 Raw spectra with D, G, D′, and G′ Raman bands identified in pitch-based Nippon Graphite Fibers using an excitation wavelength of 752 nm [11]

polycrystalline graphite was found at ~1,330 cm^{-1} and can be related to the boundaries of the graphite crystals. Thus, this peak could be related to the particle size and structural disorder effects (Figs. 5.6 and 5.7) [11, 12].

5.2.6 Auger Electron Spectroscopy

An alternative method for chemical surface analysis is Auger electron spectroscopy (AES). During bombardment of the surface under investigation with a beam of

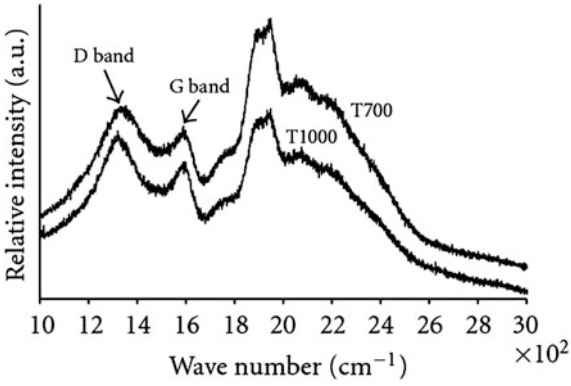

Fig. 5.7 Raw spectra with D and G Raman bands identified in polyacrylonitrile (PAN)-based fibers using an excitation wavelength of 752 nm [11]

electrons in the energy range 1–5 keV, vacancies are created in the core level. These vacancies represent excited ions in the surface region, which may undergo de-excitation, resulting in the creation of Auger electrons. Each electron has energy characteristic to a specific element. By analyzing all back-scattered Auger electrons in the energy range 0–1 keV, a complete picture of the elemental composition of the outermost atomic layers is obtained. The surface sensitivity originates from the fact that the escape depth of electrons in the energy range 50–1,000 eV is between 0.5 and 1.5 nm. In recent years, AES is widely used in the fields of corrosion, catalysis, metallurgy, thin-film devices, and tribology [13].

5.2.7 Scanning Tunneling Microscopy (STM)

STM is based on quantum tunneling. When a conducting tip is brought in close proximity to the surface to be examined, a bias (voltage difference) applied between the two can allow electrons to tunnel through the vacuum between them. The resulting tunneling current is a function of the tip position, applied voltage, and the local density of states (LDOS) of the sample. Information is acquired by monitoring the current as the tip scans across the surface and the data are usually displayed in the form of an image. STM can be a challenging technique because it requires extremely clean and stable surfaces, sharp tips, excellent vibration control, and sophisticated electronics; nonetheless, many scientists have built their own STMs [14, 15].

Paredes et al. [15] investigated the surface modification of ultrahigh modulus carbon fibers by STM. Representative atomic-scale STM images of the fresh untreated material are presented in Fig. 5.8. In Fig. 5.8a, for example, the triangular atomic-scale pattern, typical to the STM images of the pristine graphite basal plane, can be identified. Undulations in the topography can be observed in Fig. 5.8b. Figure 5.8c shows another type of structure rather commonly encountered on the

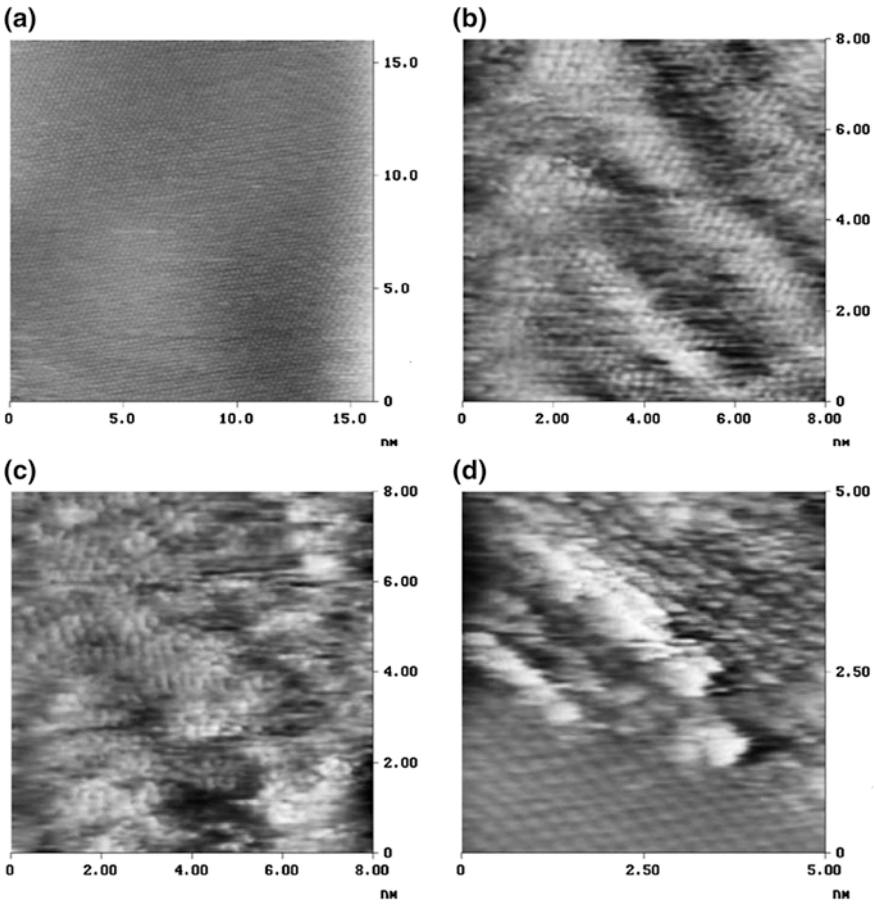

Fig. 5.8 Atomic-scale STM images of untreated ultrahigh modulus carbon fiber surface. Z scale is 3 nm [15]

untreated fiber surface. Atomic-sized spots can be distinctly perceived in this image; however, their arrangement differs from that of perfect graphite both in the long range (as observed in Fig. 5.8a) as well as locally (as in Fig. 5.8b).

5.2.8 Atomic Force Microscopy

Atomic force microscopy (AFM) or scanning force microscopy (SFM) is a very high-resolution scanning probe microscopy, which allows for characterization at resolutions on the order of fractions of a nanometer, which is more than 1,000 times better than the optical diffraction limit. The precursor to the AFM, the scanning

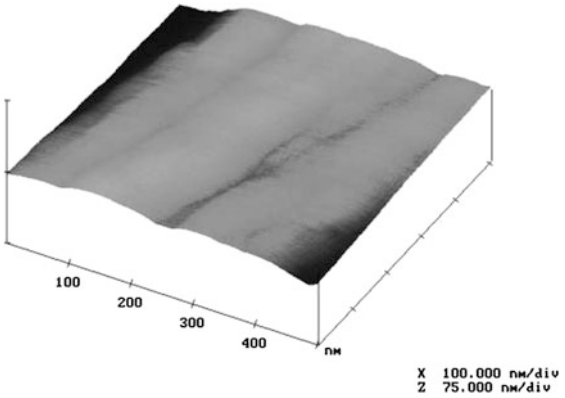

Fig. 5.9 Surface contour plot of a carbon fiber [16]

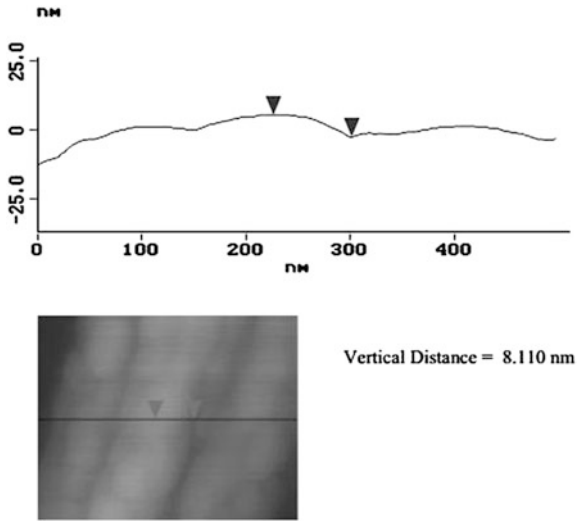

Fig. 5.10 Horizontal section plot of a carbon fiber [16]

tunneling microscope, was developed by Gerd Binnig and Heinrich Rohrer in the early 1980s at IBM Research laboratory, Zurich, which earned them the Nobel Prize for Physics in 1986. Binnig, Quate, and Gerber invented the first AFM in 1986. The first commercially available AFM was introduced in 1989. The AFM is one of the foremost tools for imaging, measuring, and manipulating matter at the nanoscale (Figs. 5.9 and 5.10) [16, 17].

Smiley and Delgass used AFM to investigate the topographical changes of carbon fibers exposed to low-temperature low-power oxygen plasma treatments (Figs. 5.11 and 5.12) [17]. Through their research, it was found that the grooves present in the AFM images of untreated fibers were the same as those seen by the SEM. The axial grooves were unevenly spaced by approximately 40–120 nm apart and showed a depth distribution ranging from 1 to 7 nm. The fibers treated with

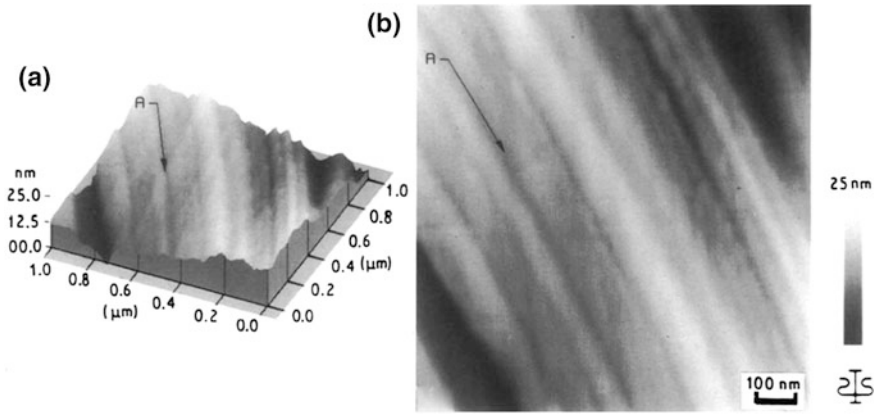

Fig. 5.11 AFM image of untreated Cellion 6000 carbon fiber. **a** Tilted view. **b** Top view [17]

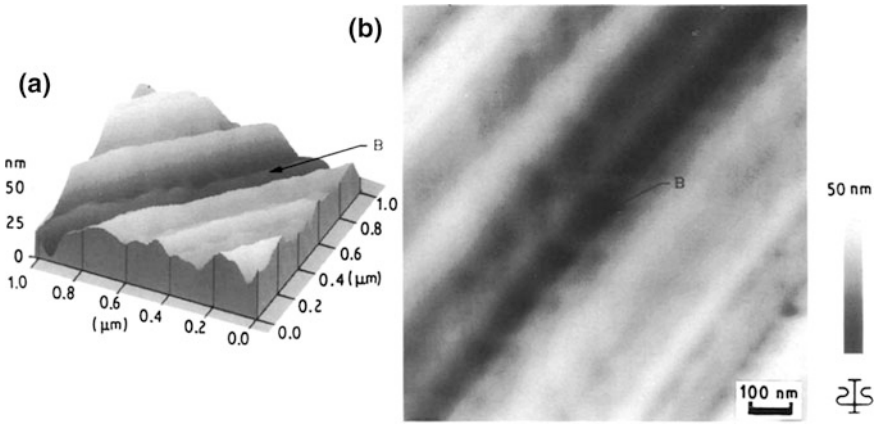

Fig. 5.12 AFM image of a Cellion 6000 carbon fiber treated in oxygen plasma for 2 min: **a** tilted view and **b** top view [17]

oxygen plasma for 2 and 15 min were also imaged by AFM. It was found that the fiber surfaces go through an initial roughening after the short treatment, followed by an overall smoothening with increase in the treatment time.

5.2.9 Titration

The potential chemical activity of surface groups on fibers may be determined by titration techniques. For example, the relative concentration of hydrolyzable groups introduced during the manufacturing or posttreatment of carbon fibers may be

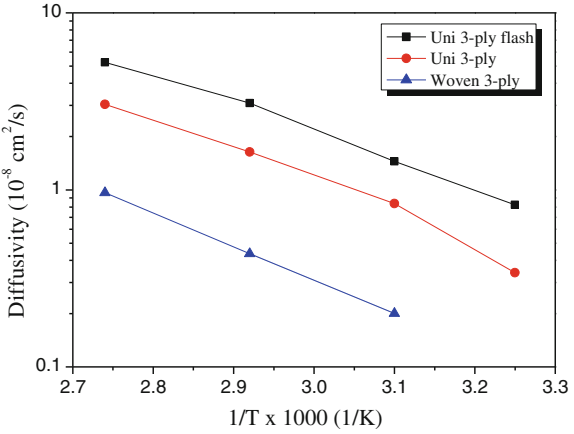

Fig. 5.13 Moisture diffusivity versus 1/T for various neat resins and composites [18]

determined by measuring the pH. However, titration techniques are typically not used on commercial carbon fibers because of the low levels of surface functional groups present.

5.2.10 Moisture Content

The moisture content or moisture regains of fibers or textiles may be determined using common methods. Care must be exercised when applying the procedure because volatile materials in addition to moisture may also be removed. If possible, tests should be performed on fibers that have not been sized. Moisture content is expressed as weight percentage moisture based on the dry weight of the specimen (Fig. 5.13).

5.2.11 Thermal Stability and Oxidative Resistance

The susceptibility of fibers and fiber surfaces to undergo oxidation is measured as the weight loss under specific conditions of time, temperature, and atmosphere. Thermogravimetric analysis (TGA) is a process that uses heat and stoichiometry ratios to determine the percent by mass of the various components. Analysis is carried out by raising the temperature of the sample gradually and plotting the weight (percentage) against temperature. The temperature in many testing methods routinely reaches 1,000 °C or greater. After the data are obtained, curve smoothing and other operations may be carried out to find the exact points of inflection.

High-resolution TGA is often employed to obtain greater accuracy in areas at which the derivative curve peaks. In this method, the temperature increase slows as

weight loss increases. This is done to more accurately identify the exact temperature at which a peak occurs. Several modern TGA devices can vent burnoff to an infrared spectrophotometer to analyze the gas composition (Table 5.5).

5.2.12 Filament Diameter

Perfect graphite has three-dimensional periodicity and belongs to the hexagonal crystal system. However, Johnson [31] reported that face-centered cubic sequence is also observed. In carbon fibers, within each basal plane of aromatic rings, the carbon atoms are placed on a hexagonal lattice, but the corresponding atoms on an adjacent plane may be translated by an arbitrary displacement. Hence, carbon fibers generally have only two-dimensional order referred to as "turbostratic" structure [32]. Interplanar spacing in carbon fibers processed even at higher temperatures is significantly higher than that of perfect graphite. However, many researchers [33–36] have reported the evidence of three-dimensional order in certain carbon fibers. Kumar et al. [33] have reported that most PAN-based carbon fibers exhibit a particulate morphology, whereas pitch-based carbon fibers exhibit a sheet-like morphology. They also reported that a sheet-like morphology does not necessarily imply a three-dimensional order; on the other hand, a fiber with particulate morphology can display three-dimensional order. Rayon-based fibers show particulate morphology and may show three-dimensional order. SEM images of PAN-based, pitch-based, and rayon-based carbon fibers are shown in Figs. 5.14, 5.15 and 5.16 [33], respectively.

Extensive graphitized small areas have been observed to exist even in fibers, which have never been exposed to temperatures beyond 1,100 °C [34]. Preferential orientation of graphitic sheets along the fiber axis increases with heat-treatment temperature. The orientation and size of these sheets are greater on the surface than in the interior of the carbon fibers [33, 34]. The modulus of the fibers increases with increase in orientation [34]. Carbon fibers are reported to consist of up to 20 % voids elongated in along the fiber axis [32]. There is a transition from many small pores to fewer larger pores with an increase in the heat-treatment temperature [35].

PAN-based carbon fibers show higher tensile and compressive strengths than pitch-based carbon fibers because PAN-based fibers consist of particle-like structures and smaller crystals in comparison with the sheet-like structure and larger crystals in pitch-based fibers [35–40]. The cross-sectional structure of carbon fibers also plays an important role in determining the compressive properties of carbon fibers. Hayes et al. [36] studied the compressive behavior of two different pitch-based carbon fibers and proposed that fibers with a folded radial texture show higher compressive strengths than fibers with a flat-layer structure. The two structures have been reproduced in Fig. 5.17 [36]. Knibbs [41] identified three different types of structures for PAN-based carbon fibers prepared under different processing conditions. The three structures are schematically represented in Fig. 5.18 [34]. The transverse structure of the final carbon fibers depends very much upon the type of spinning process used, the temperature of spinning, the shape of

Table 5.5 General condition during PAN fiber oxidative stabilization

References	Oxidative stabilization temperature (°C)	Types of stabilization process	Stretching ratio/load	Heating rate (°C/min)	Air flow rate (L/min)	Prestabilization treatment
Chen and Harrison [19]	230	Batch process, total stabilization time: 5 h	Under restrained at constant length (tow was tied at each end)	1	4	DMF solution was used as plasticizer
Wangxi et al. [20]	200–400	Batch process	Fixed-length method	2	–	–
Hou et al. [21]	300	Batch process	Free shrinkage, tow precursor was tied to Kevlar thread at both ends	5	3	–
Yu et al. [22, 23]	195–280	Continuous process: 10 separated zones, 6 min for each zone	Stretching was applied on PAN fibers by controlling speed differences between feed rollers and take-up rollers	–	–	–
Gupta and Harrison [24]	200–500, optimum temperature: 380	Batch process	Free shrink/stretch with 5-Ib load cell	1	4	–
Hou et al. [25]	200–280	Batch process, isothermal for 22 h	Free shrinkage, tow precursor was tied to Kevlar thread at both ends	2	3	–
Mathur et al. [26]	230	Batch process, isothermal for 100 min	Under restrained at a constant load (1 mg) per filament tow	5	1	CuCl solution was used as plasticizer
Wu et al. [27]	160–230	Continuous process: three separated zones	Under restrained at a constant load of 2 N	1	–	–

(continued)

Table 5.5 (continued)

References	Oxidative stabilization temperature (°C)	Types of stabilization process	Stretching ratio/load	Heating rate (°C/min)	Air flow rate (L/min)	Prestabilization treatment
Ge et al. [28]	190–275	Continuous process: 10 separated zones, 6 min for each zone, total stabilization time: approximately 60 min	5 % stretching ratio	–	–	–
He et al. [29]	190–270	Continuous process: 10 separated zones, total stabilization time: approximately 40 min	10 % stretching ratio	–	–	–
Fazlitdinova et al. [30]	245–290	Batch process, isothermal for various residence times [0.5, 1, 2, 4, 6, and 8 h]	Under restrained at a constant load of 0.6 g/tex	–	–	–

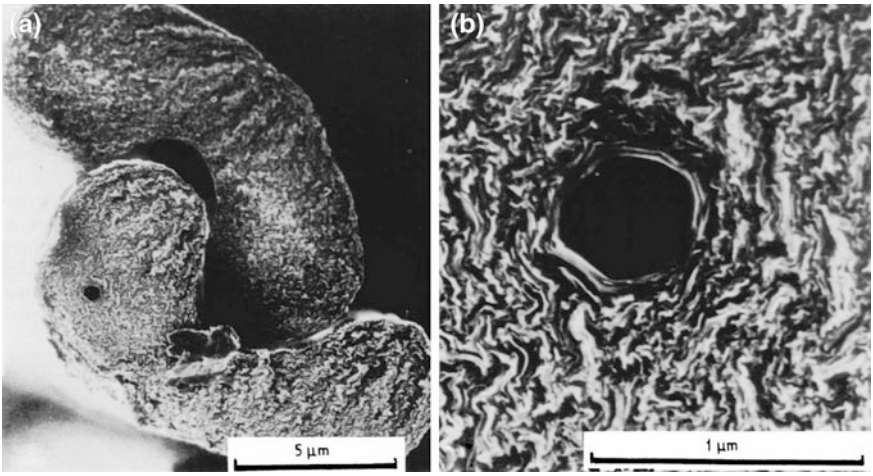

Fig. 5.14 SEM images of PAN-based carbon fibers [33] at **a** low and **b** high magnifications

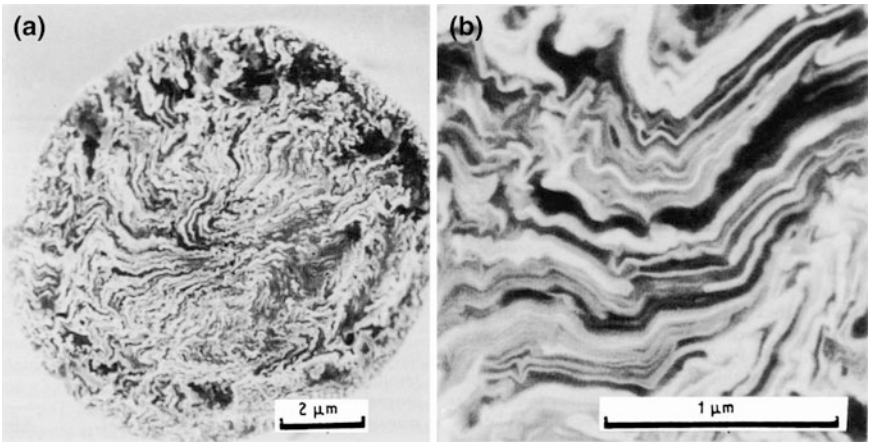

Fig. 5.15 SEM images of pitch-based carbon fibers [33] at **a** low and **b** high magnifications

the spinneret, and the use of a stirrer and its shape [34, 42]. However, the structure is independent of the heat-treatment temperature [34].

5.2.13 Electrical Resistivity

The presence of an electric field inside a material will cause the flow of an electric current. The electrical resistivity (ρ, Ω/m) is defined as the ratio of the electric field (E, V/m) to the current density (J, A/m^2) generated.

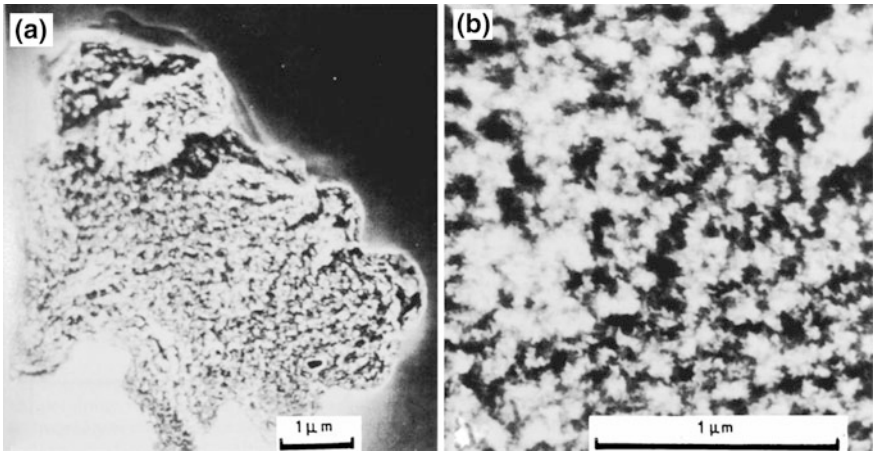

Fig. 5.16 SEM images of rayon-based carbon fibers [33] at **a** low and **b** high magnifications

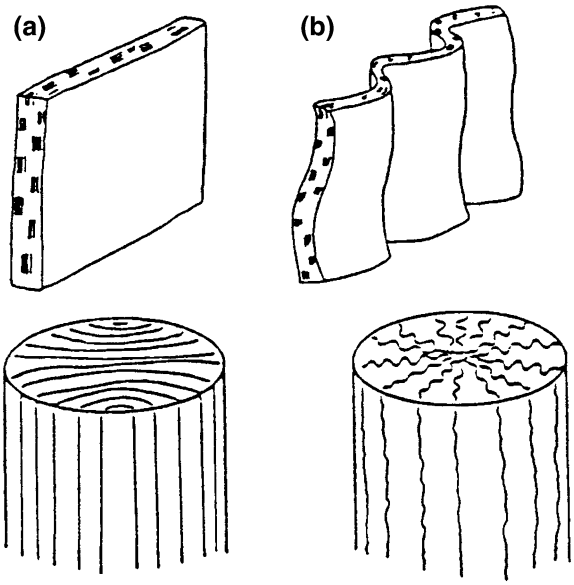

Fig. 5.17 Structure of two different pitch-based carbon fibers: **a** flat and **b** folded, proposed by Endo [36]

$$\rho = \frac{E}{J} \tag{5.2}$$

Park et al. [43] investigated the effects of the thickness of a nickel coating on the electric properties of nickel/carbon hybrid fibers. To confirm the effects of the thickness of the nickel layer on the electric resistance of the nickel/carbon hybrid fibers, the four-point probe method was employed and the results are shown in

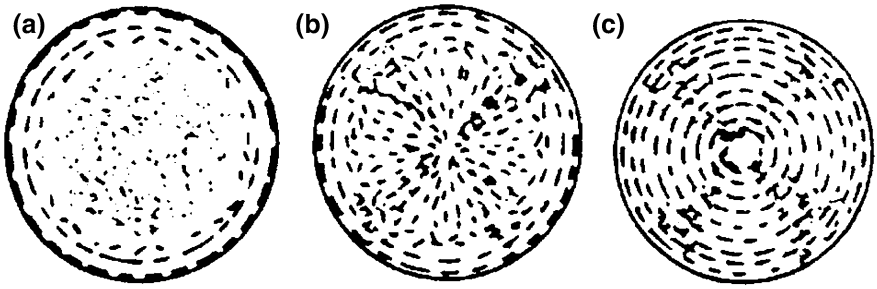

Fig. 5.18 Three different structures for PAN-based carbon fibers prepared under different processing conditions, as identified by Knibbs [41]

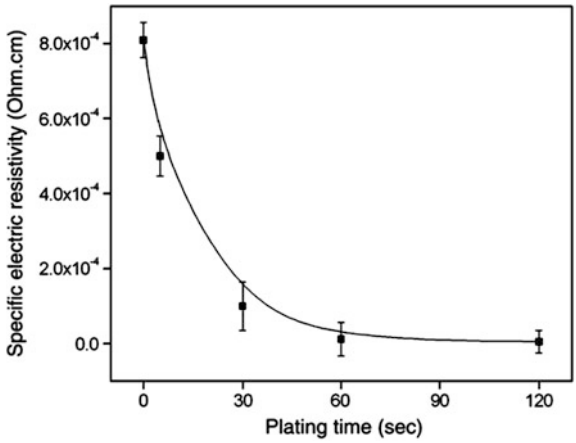

Fig. 5.19 Specific electric resistivity of Ni-plated carbon fibers as a function of plating time [43]

Fig. 5.19. The specific resistance was observed to decrease with increase in plating time. Also, while the specific resistivity of the as-received sample was higher than 0.80×10^{-3} Ω cm, the value decreased dramatically with increase in plating time to up to 60 s. From the good linearity of results in the range 5–30 s, there seems to be a strong correlation between the electric conductivity and the plating time.

5.2.14 Coefficient of Thermal Expansion

The coefficient of thermal expansion describes how the size of an object changes with change in temperature and the value represents the fractional change in size per degree change in temperature at a constant pressure. Several types of thermal expansion coefficients, including volumetric, area, and linear, have been developed. The type of coefficient used depends on the particular application and the

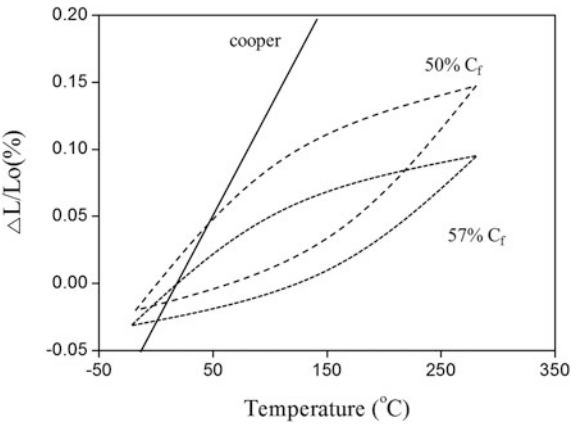

Fig. 5.20 In-plane thermal expansion of a cross-ply composite made of five layers [44]

dimensions, which are considered important. For solids, one might only be concerned with the change along a length or over some area.

Korab et al. [44] investigated the thermal expansion of cross-ply and woven carbon fiber–copper matrix composites. The in-plane thermal expansion behaviors of the cross-ply samples with and without copper foils are compared in Fig. 5.20. Samples were oriented in such a way that in three layers, fibers were parallel, and in two layers, the fibers were perpendicular to the direction of measurement. The in-plane response of the cross-ply composites is qualitatively similar to the axial response of the unidirectional specimens. Curves showed hysteresis between the heating and cooling parts of the loop, which could be ascribed to the plastic deformation of the copper matrix at higher temperatures. Further, in the case of the sample with copper foil (50 % C_f), the first loop was not closed, while in the case of the sample without copper foils (57 % C_f), all three loops were closed.

5.2.15 Thermal Conductivity

Heat transfer across materials with high thermal conductivity occurs at a higher rate than across materials with low thermal conductivity. Correspondingly, materials with high thermal conductivity are widely used in heat sink applications and materials with low thermal conductivity are used as thermal insulation. Thermal conductivity of materials is temperature dependent. The reciprocal of thermal conductivity is thermal resistivity.

Karaipekli et al. [45] investigated the improvement in the thermal conductivity of stearic acid using expanded graphite and carbon fiber additives. Figure 5.21 shows the variation of thermal conductivity of stearic acid/expanded graphite and the steric acid/carbon fiber composite phase change materials with different mass

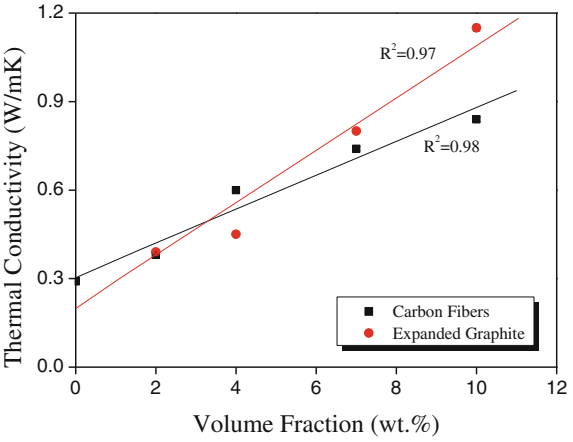

Fig. 5.21 Variation of effective thermal conductivity of stearic acid containing various volume fractions of expanded graphite and carbon fiber additives [45]

fractions of expanded graphite and carbon fibers. As clearly seen from these results, the thermal conductivity of steric acid increased with increase in the mass fraction of expanded graphite and carbon fibers.

5.2.16 Specific Heat

Specific heat is measured in a calorimeter such as that described in ASTM test method D2766 [46]. The measurement of specific heat is complex and is best left to experienced laboratories.

5.2.17 Thermal Transition Temperature

Differential scanning calorimetry, differential thermal analysis, or thermal mechanical analysis may be applied to measure the glass transition temperature (T_g) and if the fiber is semicrystalline, its crystalline melting temperature (T_m) can be measured. The general procedures for measuring T_g and T_m of organic fibers are provided in ASTM test methods D3417 and D3418 [47, 48].

5.2.18 Tensile Properties

Tensile properties are a measure of the maximum stress that a material can withstand while being stretched or pulled before necking, which is when the specimen's cross section begins to significantly contract. Tensile strength is the opposite of

compressive strength and the values can be quite different. Tensile strength is defined as stress that is measured as force per unit area. For some non-homogeneous materials (or for assembled components), it can be reported simply as a force or as a force per unit width. In the SI system, the unit is pascal (Pa) [or a multiple thereof, often megapascals (MPa)] or, equivalently, Newton per square meter (N/m^2). The customary unit is pound-force per square inch ($lbf/in.^2$ or psi) or kilopounds per square inch (ksi, or sometimes kpsi), which is equal to 1,000 psi. When measuring tensile strengths, ksi is commonly used for convenience.

5.3 Evaluation of Composites

5.3.1 Introduction

The function of the matrix in a composite is to hold the fibers in the desired position and to provide a path for introducing external loads into the fibers. Because the strengths of the matrix materials are generally lower than the fiber strengths by an order of magnitude or more, it is desirable to orient the fibers within a composite structure so that the fibers will carry the major external loads. Although the success of a composite largely relies on this, the strength and other properties of matrix materials cannot be ignored. Matrix material properties can significantly affect how a composite will perform, particularly with respect to in-plane compression, in-plane shear, resistance to impact damage, and other interlaminar behaviors, and especially when exposed to moisture and elevated temperatures.

This section focuses on methods of testing and evaluating matrix materials and their constituents. Chemical, physical, thermal, and mechanical properties are considered, in addition to methods for test specimen preparation and environmental conditioning of the test specimens.

5.3.2 Coefficient of Thermal Expansion

The thermal expansion of composite materials is an important design parameter in cryogenic technology. A large range of expansion can be achieved by varying the fiber type, content, and arrangement and the matrix. Generally, the thermal expansion of composite materials is anisotropic. For carbon fiber composites, the anisotropy results not only from the fiber arrangement but also from the fiber anisotropy. Carbon fibers show a small negative coefficient of thermal expansion in the fiber direction and a large positive coefficient perpendicular to it. For angle-plies the stresses, thermally induced between layers, strongly influence the thermal expansion behavior. In many cases, it is possible to match the thermal expansion of fiber composites to their application at least in one direction, and it should be noted

that often the same thermal expansion can be achieved by two or more different fiber arrangements. The solution with the lowest internal stresses is favored. At a fiber angle of ±30°, thermally induced stresses induce a negative expansion coefficient for carbon fiber composites. This might be useful for compensating the thermal expansion of different materials [49].

5.3.3 Thermal Conductivity

The thermal conductivity of metals, alloys, or composites with = 0, 2,…, 100 W/mK can be measured by comparative method with steady-state longitudinal heat flow from room temperature to up to approximately 1,000 °C. The comparative instrument measures heat flow based on the known thermal properties of standard reference materials. The test specimen is sandwiched between two identical reference samples. This stack is placed between two heating elements controlled at different temperatures. A guard heater is placed around the test stack to ensure a constant heat flux through the stack and to eliminate lateral heat flow losses. As heat flows from the hot element to the cold element, the temperature gradient (T/L) across the stack is measured with thermocouples. Once the specimen reaches a state of thermal equilibrium, its thermal conductivity is calculated from the following expression:

$$\lambda = \frac{LQ}{A\Delta T} \tag{5.3}$$

In the above equation, Q is the heating power of the heater. The experimental error is in the range of approximately ±10 %. The specimen geometry is cylindrical (with a diameter of 25 or 50 mm and a height of approximately 10–40 mm).

Shim et al. [50] investigated the thermal conductivity of carbon fiber-reinforced composites with various types of cross sections. Figure 5.22a, b shows the thermal conductivity of the carbon fiber-reinforced composites in the directions parallel and perpendicular to the reinforcement direction, respectively, as a function of the fiber mass fraction. From the figures, we can see that the thermal conductivity of the composites depends on three parameters, i.e., measurement temperature, fiber content, and type of fiber cross section. C-CF/EP (C-type carbon fiber-reinforced epoxy composites), in particular, shows the highest value of thermal conductivity in a direction parallel direction to the fiber, k//, while H-CF/EP (hollow-type carbon fiber-reinforced epoxy composites) shows the lowest value of thermal conductivity in the transverse direction to the fiber, k⊥. The difference between k(//, 120 °C) and k(//, 40 °C) of C-CF/EP is relatively larger than that of R-CF/EP and C-CF/EP, while the difference between k(⊥, 120 °C) and k(⊥, 40 °C) of R-CF/EP is relatively larger than that of C-CF/EP and H-CF/EP.

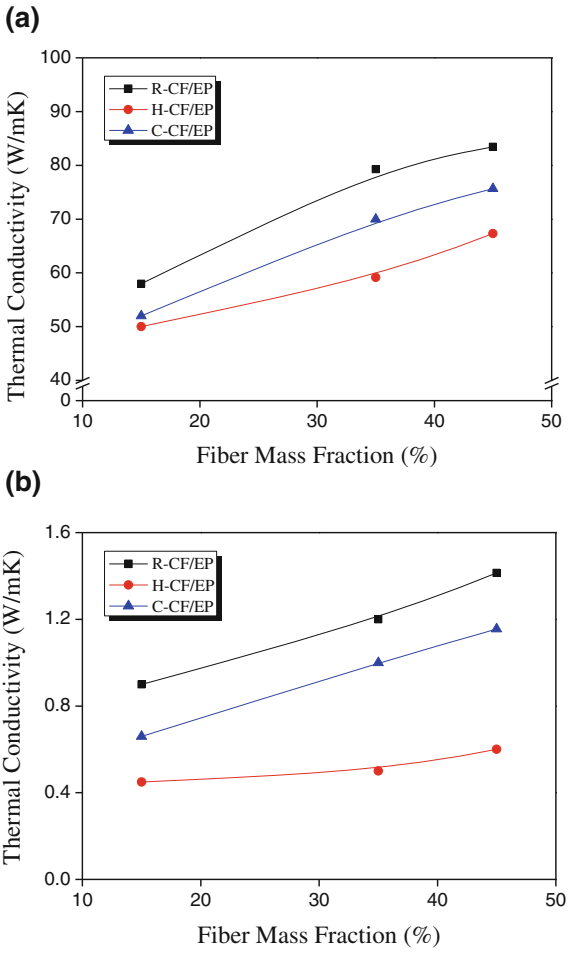

Fig. 5.22 Thermal conductivity of carbon fiber-reinforced composites in a direction **a** parallel and **b** perpendicular to that of reinforcement [50]

5.3.4 Poisson's Ratio

There is very limited information available on the Poisson's ratio of fiber-reinforced concrete. In most analytical studies, the Poisson's ratio is generally assumed to be the same as that of concrete. This may be a reasonable assumption provided the composite remains in the elastic range of behavior. As soon as cracking occurs, the confining effects of the fibers bridging the cracks will have a significant effect on the lateral deformation, and thus, the value of the measured Poisson's ratio will be affected. To the best of our knowledge, no investigation is known to have addressed this issue.

5.3.5 *Rheological Analysis*

Newtonian fluids can be characterized by a single coefficient of viscosity for a specific temperature. However, this viscosity will change with temperature, although it does not change with the flow rate or strain rate. Only a small group of fluids exhibit such constant viscosity and are known as Newtonian fluids. However, for a large class of fluids, the viscosity changes with the strain rate (or relative velocity of flow) and the fluids are termed as non-Newtonian fluids. Rheology generally accounts for the behavior of non-Newtonian fluids by characterizing the minimum number of functions that are needed to relate the stresses with the rate of change of strains or strain rates. For example, the viscosity of ketchup is reduced by shaking (or by other forms of mechanical agitation, where the relative movement of the different layers in the material actually causes a reduction in the viscosity), while that of water is not. Ketchup is a shear-thinning material because an increase in relative velocity causes a reduction in the viscosity, while some other non-Newtonian materials show the opposite behavior. That is, the viscosity increases with relative deformation, and these materials are called shear thickening or dilatant materials. Since Sir Isaac Newton drew the origins of the concept of viscosity, the study of liquids with strain rate-dependent viscosity is also often termed as Non-Newtonian fluid mechanics (Fig. 5.23).

The viscoelastic properties of polymers are determined by the effects of many variables, including temperature, pressure, and time. Other important variables include chemical composition, molecular weight and weight distribution, degree of branching and crystallinity, types of functional groups, component concentration, dilution with solvents or plasticizers, and mixture with other materials to form composite systems. Using molecular theory, the dependence of viscoelastic properties on these variables can be simplified by introducing additional concepts such as free volume, monomeric friction coefficient, and spacing between the entanglement loci to provide a qualitative understanding, and in many cases, a quantitative

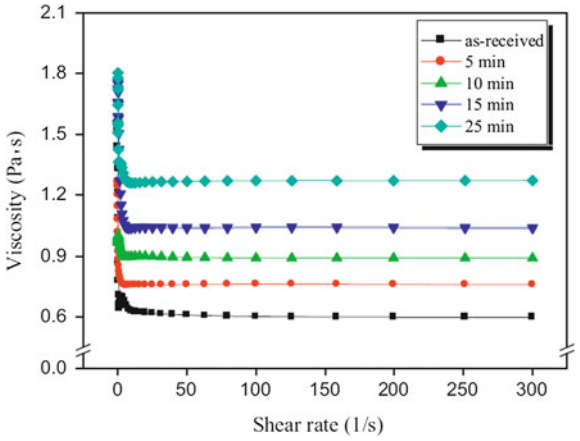

Fig. 5.23 Behavior of viscosity of Ni-coated carbon nanofibers-reinforced epoxy matrix nanocomposites [51]

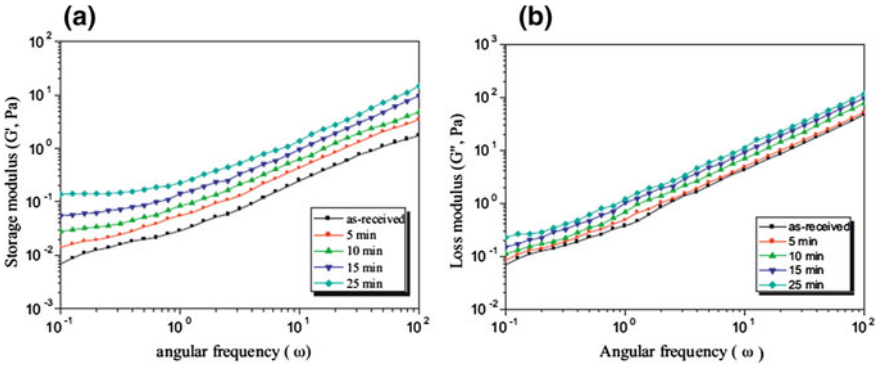

Fig. 5.24 Storage (**a**) and loss (**b**) moduli of Ni-coated carbon nanofibers-reinforced epoxy matrix nanocomposites measured with respect to angular frequency [51]

prediction of how to achieve the desired physical and chemical properties and microstructure.

Viscoelastic behavior reflects the combination of viscous and elastic responses of materials under mechanical stress, which are intermediate between liquids and solids. Fundamentally, viscoelasticity can be related to the motions of the flexible polymer molecules and their entanglements and network junctions, which forms the molecular basis of viscoelasticity. Thus, rearrangements on a local scale (kinks) are relatively rapid, while those on a long-range scale (convolutions) are very slow. In addition, a new assortment of configurations is obtained under stress. The response to the local aspects of the new distribution is rapid, while the response to the long-range aspects is slow. Thus, the range of time scales covering the response of such a system to externally applied stress is wide and continuous. By measuring the viscoelastic properties of polymers, information can be obtained about the nature and the rates of change of the configurational rearrangements and the nature of the (macro) molecular interactions over a range of time scales (Fig. 5.24).

Examples may be given to illustrate the potential applications of these principles to practical problems in the processing and use of rubbers, plastics, and fibers. Polymers are the basic materials of rubber and plastic industries and are of vital importance to textile, petroleum, automobile, paper, and pharmaceutical industries. Their viscoelastic properties determine the mechanical performance of the final products of these industries and the success of processing methods at intermediate stages of production.

In viscoelastic materials such as most polymers and plastics, the presence of liquid-like behavior depends on the properties of the applied load and hence, varies with the rate of applied load, i.e., how quickly a force is applied. The silicone toy "Silly Putty" behaves quite differently depending on the rate of application of a force. On pulling slowly, silicone exhibits continuous flow similar to that evidenced in a highly viscous liquid. Alternatively, when hit hard and directly, the material shatters like a silicate glass.

In addition, conventional rubber undergoes glass transition (often called rubber-glass transition). The Space Shuttle Challenger disaster was caused by rubber O-rings that were being used well below their glass transition temperature on an unusually cold Florida morning. The O-rings could not flex adequately to form proper seals between the sections of two solid-fuel rocket boosters.

5.3.6 Tensile Behavior

Tensile strength is the maximum stress that a material can withstand while being stretched or pulled before necking, which is when the cross section of the specimen begins to significantly contract. Tensile strength is the opposite of compressive strength and the values can be quite different (Fig. 5.25).

Tensile strengths are rarely used in the design of ductile members; however, the tensile strength is important for brittle materials. The values exhibited by common materials such as alloys, composite materials, ceramics, plastics, and wood are tabulated.

Tensile strength is defined as tress, which is measured as force per unit area. For some non-homogeneous materials (or for assembled components), the tensile strength can be reported just as a force or as a force per unit width. In the SI system, the unit of tensile strength is Pascal (Pa) [or a multiple thereof, often megapascals (MPa)] or equivalently, Newton per square meter (N/m^2). The customary unit is pound-force per square inch ($lbf/in.^2$ or psi) or kilo-pounds per square inch (ksi, or sometimes kpsi), which is equal to 1,000 psi. Kilo-pounds per square inch is commonly used for convenience when measuring tensile strengths.

Fu et al. [52] investigated the tensile properties of polypropylene composites reinforced with short-glass fibers and short-carbon fibers (i.e., SGF/PP and SCF/PP, respectively). The stress–strain curves of the SGF/PP composites and SCF/PP composites are shown in Fig. 5.26. It can be seen that the SGF/PP composites and SCF/PP composites exhibit brittle fracture and show linear deformation at lower stresses and nonlinear deformation at higher stresses. The strains at failure shown by SCF/PP composites are lower than those shown by SGF/PP composites

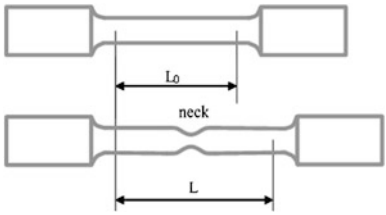

Fig. 5.25 Specimens used for tensile tests

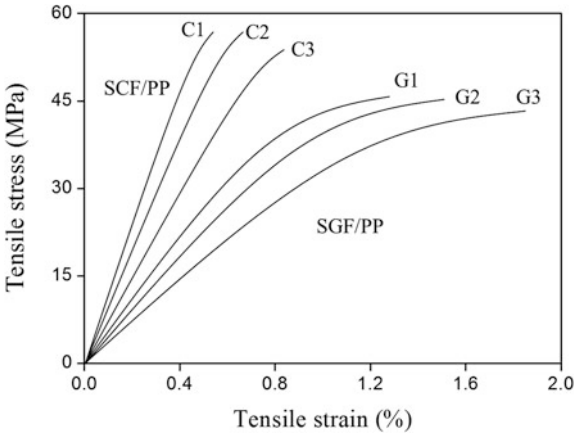

Fig. 5.26 Typical tensile stress–strain curves of SGF/PP and SCF/PP composites. SGF/PP composites: curve G1, behavior of a composite containing 25 vol.% glass fibers; curve G2, behavior of a composite containing 16 vol.% glass fibers; and curve G3, behavior of a composite containing 8 vol.% glass fibers. SCF/PP composites: curve C1, behavior of a composite containing 25 vol.% carbon fibers; curve C2, behavior of a composite containing 16 vol.% carbon fibers; and curve C3, behavior of a composite containing 8 vol.% carbon fibers [52]

5.3.7 Shear Strength

Shear strength is the strength of a material or component against the type of yield or structural failure where the material or component fails in shear. A shear load is a force that tends to produce a sliding failure on a material along a plane parallel to the direction of the force.

5.3.7.1 Interlaminar Shear Strength

The interlaminar shear strength (ILSS) is the interfacial shear stress or shear strength of the matrix materials and is measured with the three-point bend test (ASTM D2344), which is ideal for outline testing. Figure 5.27 shows a schematic of the test and shows how shear, tensile, and compressive forces are involved [53].

Park et al. [54] investigated the effect of anodization of carbon fibers on the interfacial mechanical properties of epoxy matrix composites. Figure 5.28 shows the ILSS of the carbon fiber-reinforced composites. A good relationship can be observed between the characteristics of the anodized carbon fiber surfaces and the resulting fiber matrix adhesions on the mechanical interfacial properties of the composite under the employed experimental conditions. The ILSS values increase with enhanced wettability of the fibers for adhesion at interfaces caused by the anodization, which can be attributed to the increase of the polarity of the fiber surfaces.

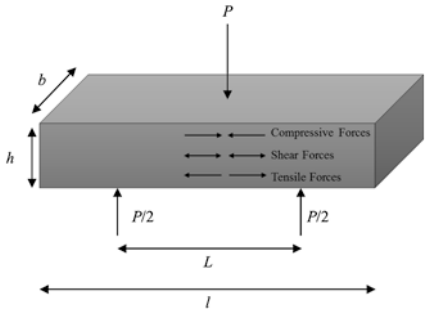

Fig. 5.27 Test configuration of a short-beam shear test [53]

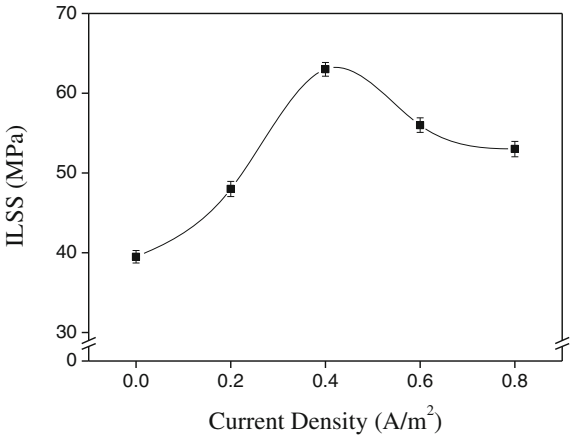

Fig. 5.28 ILSS values of carbon fiber-reinforced composites [54]

5.3.7.2 Interfacial Shear Strength

The interfacial shear strength (IFSS) is a reliable quantitative index of the adhesion between the fiber and matrix. Despite the wide application of transverse compression, double cantilever beam (DCB), and other flexural tests to measure the ILSS of the composites, single-filament composite (SFC), and microbond pull-out tests are more effective because these techniques directly measure the IFSS values of the fibers and the matrix (Fig. 5.29). Until now, most studies, which use the microbond pull-out technique, are devoted to carbon fiber/epoxy composites.

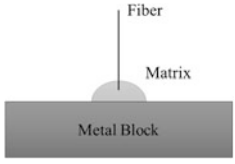

Fig. 5.29 Schematic of single fiber pull-out test specimen

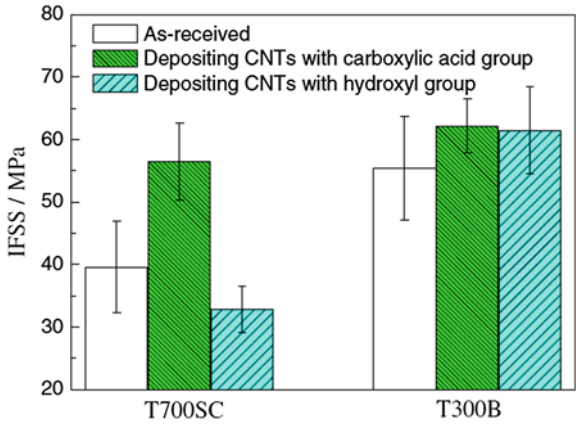

Fig. 5.30 Effects of deposited CNTs on IFSS of single fiber composites. Error bars indicate standard deviation [55]

IFSS can be calculated according to the following equation, which is based on the assumption of a constant IFSS between the fiber and its surrounding matrix [55]:

$$\text{IFSS} = \frac{F_\text{d}}{\pi d_\text{f} L_\text{e}} \tag{5.4}$$

$$= \frac{\sigma_\text{d} F_\text{d}}{4 L_\text{e}} \tag{5.5}$$

Here, F_d is the maximum fiber axial force recorded at the onset of microdroplet debonding, d_f is the fiber diameter, L_e is the embedded fiber length, and $\pi d_\text{f} L_\text{e}$ is the embedment area, and σ_d is the tensile stress at debonding.

Li et al. [55] investigated the effective IFSS of CNT-coated carbon fibers in an epoxy matrix. The IFSS of the carbon fiber/epoxy composites with and without deposited CNTs was tested by the single fiber composite fragmentation test (SFFT), and the measured data are provided in Fig. 5.30. As shown in Fig. 5.30, the deposition of the COOH–CNTs leads to a significant increase of the IFSS (approximately 43 %) for the T700SC composite. Moreover, the IFSS of the T300B composite increases by approximately 12 and 11 % after the deposition of COOH–CNTs and OH–CNTs, respectively. However, the T700SC composite shows a decrease in the IFSS by 17 % after the deposition of OH–CNTs. It was also studied the strength and interfacial shear strength of carbon fibers/poly-(phenylene sulfide) (PPS) composites with plasma surface treatments, such as oxygen, argon, and styrene plasma, by Yuan et al. [56].

5.3.8 Flexural Behavior

The flexure test method measures the behavior of materials subjected to simple beam loading. It is also called the transverse beam test with some materials. The maximum fiber stress and maximum strain are calculated for increments of load and

the results are plotted in a stress–strain diagram. Flexural strength is defined as the maximum stress in the outermost fiber. This is calculated at the surface of the specimen on the convex or tension side. Flexural modulus is calculated from the slope of the stress versus deflection curve. If the curve has no linear region, a secant line is fitted to the curve to determine the slope. There are three relevant standards, i.e., ASTM D790M, BSI 2782 Method 1005, and CRAG, and all of them cover a four-point procedure.

A flexure test produces tensile stress in the convex side of the specimen and compression stress in the concave side. This creates an area of shear stress along the midline. To ensure that the primary failure originates from the tensile or compression stress, the shear stress must be minimized. This is ensured by controlling the span to depth ratio (S/d), which is the length of the outer span divided by the height (depth) of the specimen. For most materials, an S/d of 16 is acceptable. Some materials require an S/d of 32–64 to keep the shear stress sufficiently low.

Flexure testing is often done on relatively flexible materials such as polymers, wood, and composites. There are two test types: three-point flex (Fig. 5.31) and four-point flex (Fig. 5.32). In a three-point test, the area of uniform stress is quite small and concentrated under the center loading point. In a four-point test, the area of uniform stress exists between the inner span loading points (typically half the outer span length).

For a rectangular sample under a load in a three-point bending setup,

$$\sigma = \frac{3FL}{2bd^2} \tag{5.6}$$

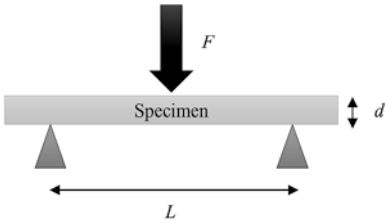

Fig. 5.31 Schematic of beam under three-point bending

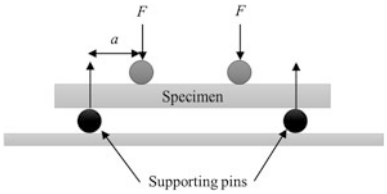

Fig. 5.32 Schematic of beam under four-point bending

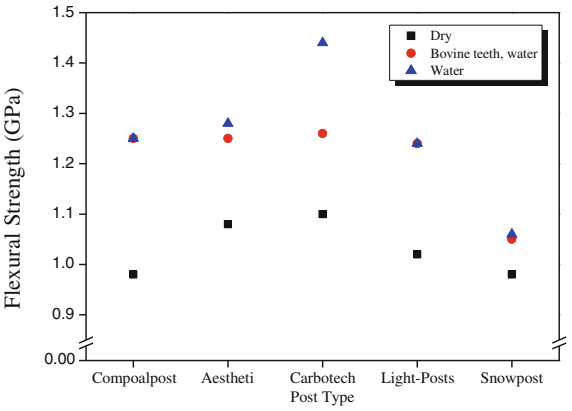

Fig. 5.33 Graphical representation showing results of flexural strength test [57]

In the above equation, F is the load (force) at the fracture point (N), L is the length of the support span (mm), b is the width (mm), and d is the thickness (mm).

For a rectangular sample under a load in a four-point bending setup,

$$\sigma = \frac{3Fa}{bd^2} \tag{5.7}$$

In the above equation, F is the load (force) at the fracture point (N), a is the distance between the supporting and loading pins (mm), b is the width (mm), and d is the thickness (mm).

Mannocci et al. [57] investigated the structure of the posts by confocal microscopy, and to evaluate the flexural strength of fiber posts stored under different conditions, a three-point bending test was used simultaneously to observe the failure mode of the posts by confocal microscopy (Fig. 5.33).

5.3.9 Uniaxial Compressive Behavior

Compressive strength is the capacity of a material or structure to withstand axially directed pushing forces. It provides data (or a plot) of force versus deformation for the conditions used in a test. When the limit of compressive strength is reached, brittle materials are crushed.

Kumar et al. [58] investigated that the uniaxial compression behavior of adhesively bonded composite scarf-joints. Figure 5.34 shows the typical geometry of our compression test specimens. These were 12.5 mm wide and had a gauge length of 10 mm in order to ensure that there was a compromise between the need to overcome Euler macrobuckling and end-tab effects. If the gauge length was too short, the end-tabs would become too close to each other and will not allow uniform distribution of stresses in the central region.

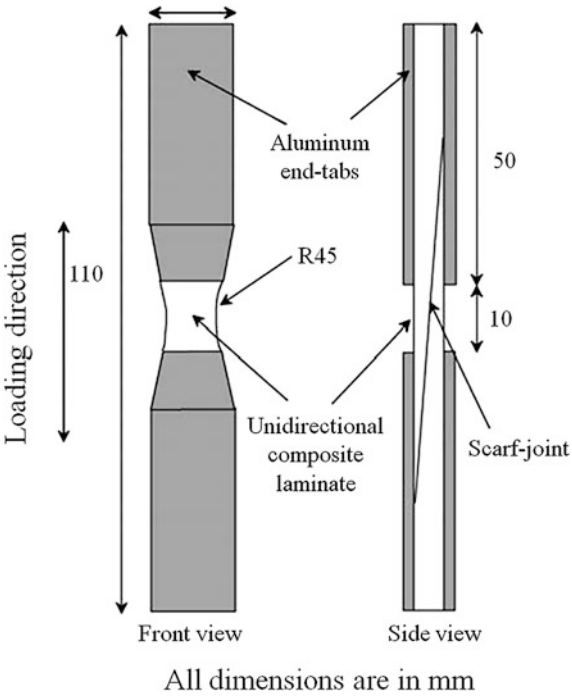

Fig. 5.34 A typical adhesively bonded scarf-joint specimen geometry used for compression testing [58]

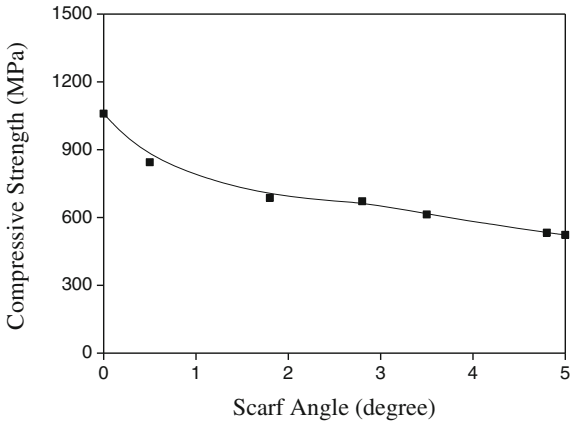

Fig. 5.35 Experimental data showing variation of composite scarf-joint strength in compression [58]

Figure 5.35 shows the unidirectional compressive scarf-joint strength as a function of scarf-angle, θ. As shown by Fig. 5.35, smaller (i.e., steeper) scarf-angles yielded higher compressive joint strengths compared to those with larger scarf-angles.

The knockdown in compressive strength is most prominent for scarf-joint angles less than about 1°. As the scarf-angle of the joint increases, the additional reduction in compressive strength becomes more gradual.

5.3.10 Fatigue

Fatigue is determined under cyclic loading when a crack is initiated and then grows to a critical size to result in failures occurring at stresses below the values obtained for normal static tests. In general, any static test adopted for fatigue testing is much more demanding. The shape of the test specimen is chosen to fail within the gage length in a manner akin to the failure of a structural component. Fatigue tests can be undertaken in the tensile, flexural, compression, and shear modes and are generally carried out in a servo-hydraulic test machine. Optical microscopy, ultrasonics, X-ray, and infrared thermography are used for detecting the onset and study of fatigue failure [53].

Khan et al. [59] investigated the fatigue damage behaviors of carbon fiber-reinforced epoxy composites containing nanoclay. Figure 5.36 shows the damage index, D, plotted as a function of the fatigue cycles for hybrid composites containing different clay contents. It can be seen that at the early stage of fatigue (say 0–12,500 cycles), the hybrid composites in general exhibited marginally more damage than the neat composites. After the initial damage period, the hybrid composite specimens sustained a relatively longer stable period with low damage indices for the rest of their fatigue life. The final failure took place much earlier in the neat composite than in the clay-CFRP hybrid composites. Further, the higher the clay content, the longer was the fatigue life, with the exception of hybrid composites containing 5 wt% clay. The diminishing improvement in fatigue life in the case of composites with clay contents higher than 3 wt% is attributed to the higher possibility of the formation of unwanted agglomerates of a relatively large size.

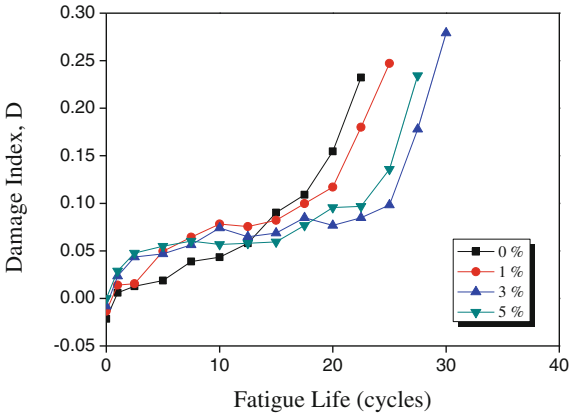

Fig. 5.36 D plotted as a function of fatigue life [59]

5.3.11 Creep

The application of a force to a material over a sustained period of time induces creep and if this force eventually leads to cracking, fracture, or rupture, the process is termed as stress cracking, static fatigue, or creep rupture. Further, if the environment speeds up the process, the rupture is termed as environmental stress cracking. The creep of a composite material will depend on the reinforcement and the matrix. Carbon fibers are not significantly affected by creep, although some loss of strength can be expected to occur under sustained loading. However, the matrix will exhibit creep, and a thermoplastic will exhibit creep to a higher extent than a thermosetting resin. However, if the fiber is well aligned in a unidirectional composite, it will have good resistance to creep along the fiber axis, although it would display creep during torsion and flexure. Plastics do tend to recover when the stress is removed, as long as no damage has occurred [53].

5.3.12 Impact Behavior

The Izod impact test is shown schematically in Fig. 5.37. The test setup and procedure are similar to those outlined above. In the Izod test, the specimen is clamped in the vertical plane as a cantilever beam and impacted by a swinging pendulum at the unsupported end. The test suffers similar problems to those reported above and again is best suited as a tool for ranking the impact resistance of composite materials.

The Charpy impact test is a standardized high strain-rate test, which determines the amount of energy absorbed by a material during fracture (Fig. 5.38). The specimen is supported in a horizontal plane and impacted by a swinging pendulum directly opposite the notch. The energy dissipated during impact is usually recorded by a dial on the test apparatus. Further information can be obtained by instrumenting the impactor with a strain gauge, thereby enabling the determination of the

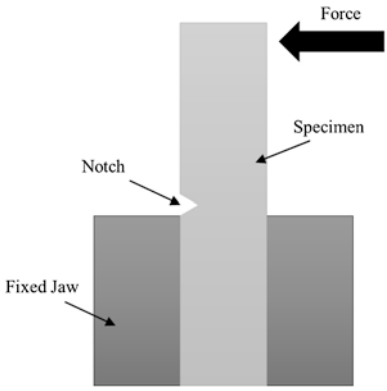

Fig. 5.37 Izod impact test

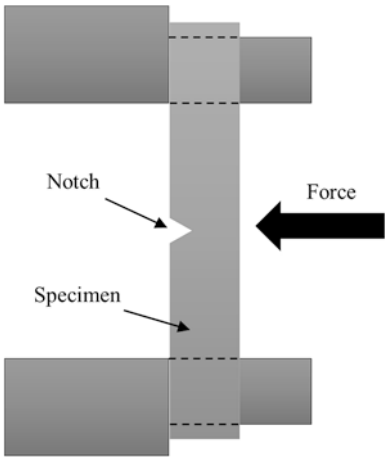

Fig. 5.38 Charpy impact test

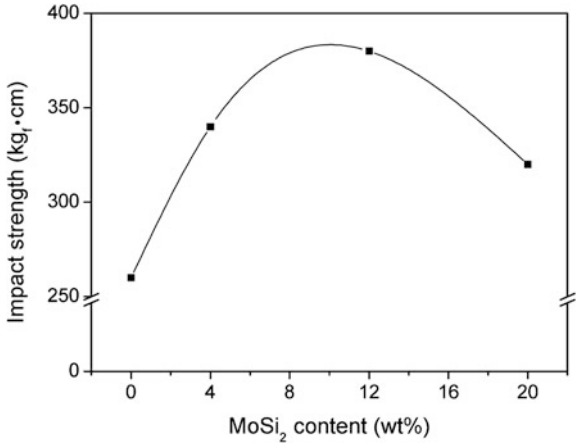

Fig. 5.39 Impact strength of C/C composites as a function of $MoSi_2$ content in prepreg resin [61]

variation of the impact force with time. The energy absorbed during impact can also be determined by integrating the force/time signal.

Therefore, the low-velocity impact test is performed with a drop-weight impact tester instead of Izod and Charpy tests [60]. Park et al. [61] investigated the impact strength of C/C composites as a function of the $MoSi_2$ content in the prepreg resin using a drop weighting impact tester. The impact properties of C/C composites are improved on increasing the $MoSi_2$ content, which coincides with the results obtained for fracture toughness. Hence, the C/C composites with $MoSi_2$ affect the impact damage conditions in comparison with composites without $MoSi_2$. During impact damage in C/C composites with low-velocity impact (1.8 m/s), the damage zone acts as a soft region within a stiff laminate and magnifies the stress locally because of matrix cracking, fiber debonding delamination, and fiber fracture (Fig. 5.39).

5.3.13 Fracture Toughness

The fundamental fracture events occurring in the fragmentation test are illustrated in Fig. 5.40. In the initial state (0), there is no damage, and the specimen compliance is C_0. The energy released by the first fiber fracture, G, is determined from the difference in the specimen compliance after (1) and before the first fiber fracture (i.e., C_1–C_0). The second fracture state (2) considers the debonding, which follows the first fiber fracture. An expression for G for debonding, which occurs subsequent to a fiber break can be derived in terms of the compliance difference between C_2 and C_1. Finally, in the third state (3), the specimen is supposed to be unloaded and then loaded again until the existing debonding begins to grow. The energy release rate, G_d, corresponding to growth of the debonding after unloading and reloading the specimen is determined from the compliance change (i.e., C_3–C_2). One important condition for this analysis is that the debonding grows before further fiber breakage occurs in the single fiber fragmentation test specimen [62].

The expression for the calculation of mode-II critical strain energy release rate, G_{IIC}, was derived from the Irwin and Kies expression for fracture energy [63, 64] as follows:

$$G_C = \frac{P^2}{2W} \cdot \frac{dC}{da} \tag{5.9}$$

In the above equation, P is the load, C is the compliance (displacement/load = δ/P), and a is the crack length. In this study, G_{IIC} was calculated using the direct beam theory method [63, 64], which used the end notched flexure (ENF) compliance expression given by [63, 65] the following equation:

$$C = \frac{2L^3 + 3a^2}{8E_f Wh^3} \tag{5.10}$$

In the above equation, L is the half-span length, a is the crack length, E_f is the flexural modulus, and h is the half the specimen thickness. From (5.9) and (5.10), with a as the sole variable for C, the following equation can be obtained:

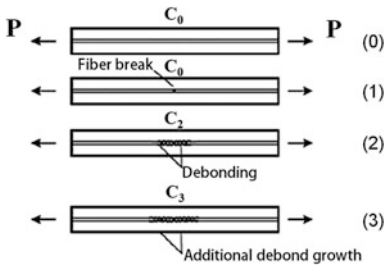

Fig. 5.40 Schematic of fracture events and associated compliances of SFFT specimen [62]

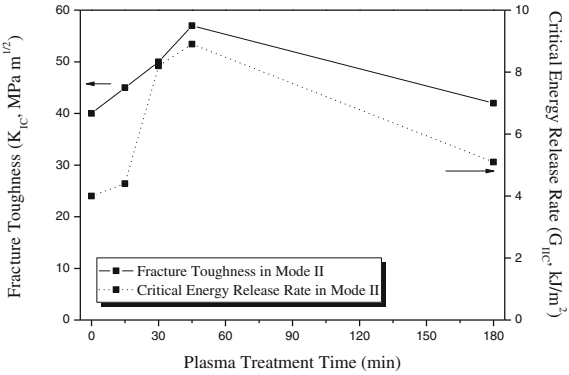

Fig. 5.41 **a** Typical load–displacement ENF curves and **b** fracture toughness and critical energy release rate in Mode-II interlaminar fracture tests for carbon fiber-reinforced epoxy matrix composites along the fiber direction [66]

$$G_{\mathrm{IIC}} = \frac{9a^2P^2}{16EW^2h^3}. \tag{5.11}$$

For beams under small deflection, an expression for E can be obtained from (5.10), which may be substituted into (5.11), yielding (5.12).

$$G_{\mathrm{IIC}} = \frac{9a^2P\delta}{2W(2L^3 + 3a^3)} \tag{5.12}$$

The maximum load was used as the critical load PC to determine the critical energy release rate and fracture toughness.

Figure 5.41 shows the typical relationship between the load and displacement at the central loading point of the ENF specimens. Elastic behavior is observed in the ENF specimens. Therefore, the maximum load is used as the critical load to determine the critical energy release rate and fracture toughness.

5.4 Relationship Between Surface and Interfacial Properties in Composites

5.4.1 Surface Free Energy and Work of Adhesion

It is well known that the knowledge of surface energetics at a given temperature of a solid has recently allowed significant progress in many academic and scientific fields involving two nonidentical molecular interactions at a certain intermolecular distance, such as adsorption (gas–solid), wettability (liquid–solid), and adhesion (solid–solid). The surface free energy or surface tension (r_s) of a solid (subscript S)

can be expressed by the sum of the London dispersive ($r_S{}^L$) and specific (or polar, $r_S{}^{SP}$) components.

$$r_s = r_S{}^L + r_S{}^{SP} \tag{5.13}$$

The superscripts L and SP are the components of the surface free energy resulting from intermolecular interactions of the London force of van der Waals attraction and the specific force (Debye, Keesom, hydrogen bonding, and other small polar effects), respectively. When the surface free energy of a solid can be determined on the basis of the contact angle measurements using the geometric mean, the work of adhesion, W_A, according to the Fowkes' proposition [89] based on the solid (S)–liquid (L) droplet–air system, can be described by the following equation:

$$W_A = \gamma_L(1 + \cos\theta) \tag{5.14}$$

$$= 2\sqrt{\gamma_L{}^L \cdot \gamma_S{}^L} + 2\sqrt{\gamma_L{}^{SP} \cdot \gamma_S{}^{SP}} \tag{5.15}$$

θ is the contact angle of a liquid droplet in the solid state. For use on a large variety of polar solids, at least two nonidentical liquids with polar surface energies, such as water, diiodomethane, ethylene glycol, and glycerol, are needed if the values of r_L^L and $r_L{}^{SP}$ are known.

Park et al. [61] investigated the effects of the MoSi content on the work of adhesion of the C/C composites. In Fig. 5.42, the MoSi filler increases the work of adhesion, which is strictly influenced by the London dispersive component, $W_A{}^L$. In each case, it can also be seen that $W_A{}^L$ is more predominant than the specific component ($W_A{}^{SP}$) with respect to the work of adhesion of the composites. This is due to the carbonaceous nature of the composites caused by the decrease of oxygen functional groups, since carbonization leads to a very low content of oxygen.

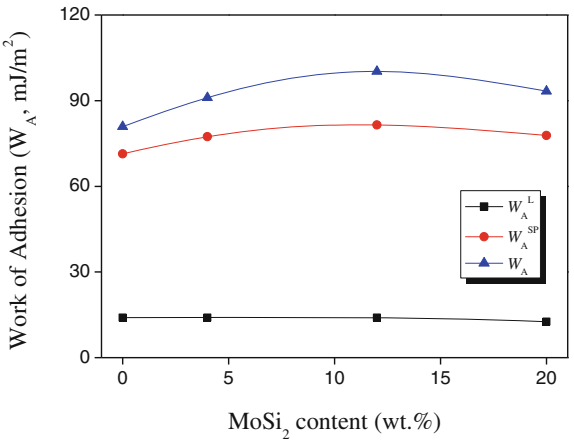

Fig. 5.42 Work of adhesion (W_A) of C/C composites as a function of MoSi content of the prepreg resin [61]

5.4.2 Surface Free Energy Analysis Using Linear Fit Method

The wettability of carbon fibers was determined by measuring the wicking rates either by the mass pickup technique or by the surface velocity method. The contact angle used in this investigation was then calculated using Washburn's equation [67, 68], which defines the flow of a liquid through a capillary as follows:

$$\frac{m}{t} = \frac{c \cdot \rho_2 \cdot \gamma_L \cdot \cos\theta}{2\eta} \tag{5.16}$$

In (5.16), m is the weight of the penetrating liquid, t is the flow time, c is the packing factor, γ_L is the surface tension of liquid, and η and ρ_2 are the liquid density and viscosity, respectively. The London dispersive and specific components of surface free energy of carbon fibers are determined by measuring the contact angles of a variety of testing liquids with known London dispersive and specific components and by analyzing the results in accordance with the method proposed by Owens and Wendt [69] and Kaelble [70], using the geometric mean.

$$\frac{\gamma_L(1-\cos\theta)}{2(\gamma_L{}^L)^{1/2}} = (\gamma_S{}^{SP})^{1/2} \cdot \left(\frac{\gamma_L{}^{SP}}{\gamma_L{}^L}\right)^{1/2} + (\gamma_S{}^L)^{1/2} \tag{5.17}$$

In the above equation, the subscripts L and S, respectively, represent the liquid and solid states, $\gamma_L{}^L$ represents the London dispersive component, and $\gamma_L{}^{SP}$ corresponds to the specific component.

Park et al. [71] investigated the surface free energies and their oxyfluorinated carbon fiber components are listed in Table 5.6. A decrease in the surface free energies is observed. The higher the fluorine content on the carbon fiber surfaces, the weaker the surface free energies. In other words, seemingly the polar component of the surface free energy increases at higher degrees of fluorination, and then decreases slightly again for lower degrees of fluorination and with increasing fluorination temperatures. All of the experimental results listed in Table 5.6 are those usually observed for fluorinated carbon materials, considering that C–F bonding varies from chemical to physical bonding with increasing fluorination temperatures (for CFx prepared at 100 °C or higher).

Table 5.6 Surface free energy (γ_S), London dispersive ($\gamma_S{}^d$), and specific ($\gamma_S{}^p$) component of oxyfluorinated carbon fibers as functions of oxyfluorination condition (unit: mJ m^{-2}) [71]

Specimens	$\gamma_S{}^d$	($\gamma_S{}^p$)	γ_S	X_p
As-received	40.35	3.06	43.41	0.07
CFO-RT	30.80	8.61	39.41	0.22
CFO-100	29.70	11.68	41.38	0.28
CFO-300	28.62	9.51	38.13	0.25
CFO-400	28.45	9.10	37.55	0.24

5.4.3 Weibull Distribution

Both the tensile and pull-out strength of carbon fibers are usually assessed by single filament tensile tests [72]. The experimental data generated by these tests have high scatter, mainly because of the presence of flaws along the fibers. Thus, the interpretation of the data must be done statistically. Several statistical distributions have been used to describe the tensile data, the most flexible so far being the Weibull distribution [73, 74].

$$F(\sigma;\sigma_0,m) = 1 - \exp\left(-\left(\frac{\sigma}{\sigma_0}\right)^m\right) \tag{5.18}$$

In (5.18), σ is the load factor, σ_0 is the Weibull scale, and m represents the shape parameters. The flaw-induced nature of fiber failure leads to a length dependence of its tensile strength, i.e., the longer the fiber length, the larger the number of flaws that are present and the higher is the probability of occurrence of a severe flaw. The Weibull distribution has to be adapted to account for this dependence.

This also assumes that the strength distribution of each independent link is described by a simple Weibull distribution characterized by identical parameters. This leads to fiber survival probabilities equal to the product of the survival probabilities of each link. On the basis of these considerations, the Weibull cumulative distribution function F (σ; σ_0, m) and the corresponding mean Weibull strength ($\overline{\sigma}$), adapted to account for the gauge length dependence of the fibers (L), may be described by the following equations:

$$F(\sigma;\sigma_0,m) = 1 - \exp\left(-L\left(\frac{\sigma}{\sigma_0}\right)^m\right) \tag{5.19}$$

$$\overline{\sigma} = \sigma_0 L^{-1/m}\Gamma\left(1+\frac{1}{m}\right) \tag{5.20}$$

In the above equation, Γ is the gamma function.

The parameter estimate for the two-parameter Weibull distribution is made for the strength data obtained at all gauge lengths simultaneously. In this work, the maximum likelihood theory is used to determine the Weibull parameters. The method used is described in Stoner's thesis [75] and in the calculation programs explained in the thesis. In this way, for each type of fiber, a single set of parameters is obtained that fits all the gauge lengths tested [76]. The estimate of the tensile strength at any gauge length needed for the interfacial shear strength calculations is performed simply by substituting the calculated parameters into (5.20), for the specified fiber length.

Also, the load factor (σ) and L taken as part of the σ_0 parameter are redefined with the unit of stress (MPa) such that the Weibull distribution function can be expressed as follows:

$$P = 1 - \exp[-(\sigma/\sigma_0)^m] \tag{5.21}$$

By taking logarithm of the survival probability $(1 - P)$ twice, we also obtained the following equation:

$$\ln\ln[1/(1-P)] = m\ln(\sigma) + \ln[(1/\sigma_0)^m] \tag{5.22}$$

The parameters m and σ_0 defining the Weibull distribution are usually determined either graphically or numerically by the least-squares method. Therefore, we can assign a failure probability P_i to each value of σ_i after ranking all the measured values in ascending order (i taking values from 1 to n, which corresponds to the number of measurements of the sample tested), according to one of the principal probabilities used.

$$P = i/(n+1) \tag{5.23}$$

After the tensile and pull-out tests on the carbon fibers, Park et al. [77] ordered the fracture strength values for each sample and assigned a probability P_i to each value σ_i using (5.22). The different cumulative probability distributions are shown in Fig. 5.43. For an initial failure probability at 6 %, the fracture strength is increased from 5.6 MPa for the as-received state to 10.9 MPa after a 1.0 keV Ar^+ ion treatment. The distributions for entire Ar^+ ion-irradiated carbon fibers are comparably closer to each other, with the exception of a few high extreme values. Also, the Weibull parameter m and the scale parameter σ_0 of all the ion-irradiated carbon fibers after pull-out tests exhibit similar behavior, compared with as-received carbon fibers, as

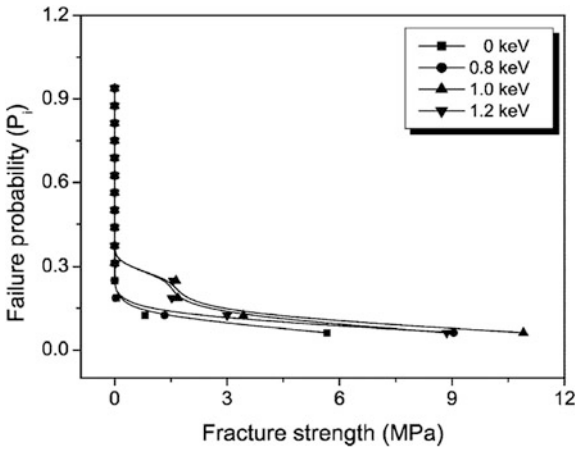

Fig. 5.43 Relationship between the failure probability and fracture strength in Ar^+ ion-irradiated carbon fibers [77]

Table 5.7 Maximum IFSS (τ_{max}), interfacial toughness (G_i), and Weibull distribution parameters of a single carbon fiber with different ion beam irradiations [77]

Ion beam energy (keV)	τ_{max} (MPa)	G_i (kJ)	Parameter (m)	Scale parameter (σ_0)
0	5.65	9.25	2.66	1.43×10^{-2}
0.8	9.04	12.77	2.41	1.22×10^{-2}
1.0	10.90	14.33	2.25	1.16×10^{-2}
1.2	8.86	11.76	2.17	1.24×10^{-2}

listed in Table 5.7. This means that the interfacial shear strength (τ) or failure strength of Ar^+ ion-irradiated single-filament carbon fiber is dependent on the failure mechanism of carbon fibers in an epoxy matrix system.

References

1. P.M.A. Sherwood, J. Electron Spectrosc. Relat. Phenom. **81**, 319 (1996)
2. Y.Y. Li, K. Mochidzuki, A. Sakoda, M. Suzuki, Carbon **39**, 2143 (2001)
3. J.C. Vickerman, I.S. Gilmore, B.D. Ratner, D.G. Castner, *Surface Analysis—The Principal Techniques*, 2nd edn. (Wiley, New York, 2009)
4. J.M. Walls, *Methods of Surface Analysis* (Cambridge University Press, Australia, 1989)
5. ASTM D 3178, *ASTM Book of Standards* (ASTM, Philadelphia, 1984)
6. ASTM D 3174, *ASTM Book of Standards* (ASTM, Philadelphia, 1984)
7. D. Briggs, M.P. Seah, *Practical Surface Analysis by Auger and X-ray Photoelectron Spectroscopy* (Wiley, Chichester, 1983)
8. J.P. Eberhart, *Structural and Chemical Analysis of Materials* (Wiley, New York, 1991)
9. T. Wang, P.M.A. Sherwood, Chem. Mater. **6**, 788 (1994)
10. N. Iwashita, C.R. Park, H. Fujimoto, M. Shiraishi, M. Inagaki, Carbon **42**, 701 (2004)
11. G. Washer, F. Blum Jr, Adv. Mater. Sci. Eng. **2008**, 693207 (2008)
12. N. Melanitis, P.L. Tetlow, C. Galiotis, J. Mater. Sci. **31**, 851 (1996)
13. F. Hopfgarten, Fibre. Sci. Technol. **11**, 67 (1978)
14. H.J. Jacobasch, K. Grundke, P. Uhlmann, F. Simon, E. Mader, Compos. Interfaces **3**, 293 (1996)
15. J.I. Paredes, A. Martínez-Alonso, J.M.D. Tascón, J. Colloid Interface Sci. **258**, 276 (2003)
16. Z. Dai, B. Zhang, F. Shi, M. Li, Z. Zhang, Y. Gu, Appl. Surf. Sci. **257**, 8457 (2011)
17. R.J. Smiley, W.N. Delgass, J. Mater. Sci. **28**, 3601 (1993)
18. L.R. Bao, A.F. Yee, Polymer **43**, 3987 (2002)
19. J.C. Chen, I.R. Harion, Carbon **40**, 25 (2002)
20. W. Zhang, L. Jie, J. Liang, J. Mater. Sci. Technol. **20**, 369 (2004)
21. Y. Hou, T. Sun, H. Wang, D. Wu, J. Text. Res. **78**, 806 (2008)
22. M.J. Yu, C.G. Wang, Y.J. Bai, Y.X. Wang, Q.F. Wang, H.Z. Liu, Polym. Bull. **57**, 525 (2006)
23. M.J. Yu, Y.J. Bai, C.G. Wang, Y. Xu, P.Z. Guo, Mater. Lett. **61**, 2292 (2007)
24. A. Gupta, I.R. Harrion, Carbon **35**, 809 (1997)
25. Y. Hou, T. Sun, H. Wang, D. Wu, J. Mater. Sci. **43**, 4910 (2008)
26. R.B. Mathur, T.L. Dhami, O.P. Bahl, Polym. Degrad. Stab. **14**, 179 (1986)
27. G. Wu, C. Lu, L. Ling, A. Hao, F. He, J. Appl. Polym. Sci. **96**, 1029 (2005)
28. H. Ge, H. Liu, J. Chen, C. Wang, J. Appl. Polym. Sci. **113**, 2413 (2009)
29. D.X. He, C.G. Wang, Y.J. Bai, N. Lun, B. Zhu, Y.X. Wang, J. Mater. Sci. **42**, 7402 (2007)

30. A.G. Fazlitdinova, V.A. Tyumentsev, S.A. Podkopayev, G.P. Shveikin, J. Mater. Sci. **45**, 3998 (2010)
31. W. Johnson, *Strong Fibers* (Elsevier, Amsterdam, 1985)
32. S. Damodaran, P. Desai, A.S. Abhiraman, J. Text. Inst. **81**, 384 (1990)
33. S. Kumar, D.P. Anderson, A.S. Crasto, J. Mater. Sci. **28**, 423 (1993)
34. J.B. Donnet, R.C. Bansal, *Carbon Fibers* (Marcel Dekker, New York, 1990)
35. H. Shinohara, T. Sato, F. Saito, J. Mater. Sci. **28**, 6611 (1993)
36. G.J. Hayes, D.D. Edie, J.M. Kennedy, J. Mater. Sci. **28**, 3247 (1993)
37. M. Furuyama, M. Higuchi, K. Kubomura, H. Sunago, ibid. **28**, 1611 (1993)
38. M.G. Northolt, L.H. Veldhuizen, H. Jansen, in *Proceedings of 20th Biennial Conference on Carbon* (American Carbon Society, 1991), p. 222
39. V.R. Mehta, S. Kumar, J. Mater. Sci. **29**, 3658 (1994)
40. H.J. Jacobsch, K. Grundke, P. Uhlmann, F. Simon, E. Maeder, Comp. Interfaces **3**, 293 (1996)
41. R.H. Knibbs, J. Microsc. **94**, 273 (1971)
42. M.S. Dresselhaus, G. Dresselhaus, K. Sugihara, I.L. Spain, H.A. Goldberg, *Graphite Fibers and Filaments* (Springer, Berlin, 1988)
43. B.J. Kim, W.K. Choi, M.K. Um, S.J. Park, Surf. Coat. Tech. **205**, 3416 (2011)
44. J. Korab, P. Stefanik, S. Kavecky, P. Sebo, G. Korb, Comp. A **33**, 133 (2002)
45. A. Karaipekli, A. Sari, K. Kaygusuz, Renewable Energy **32**, 2201 (2007)
46. ASTM D 2766, *ASTM Book of Standards* (ASTM, Philadelphia, 1984)
47. ASTM D 3417-83, *ASTM Book of Standards* (ASTM, Philadelphia, 1984)
48. ASTM D 3418-82, *ASTM Book of Standards* (ASTM, Philadelphia, 1984)
49. G. Schwarz, F. Krahn, G. Hartwig, Cryogenics **31**, 244 (1991)
50. H.B. Shim, M.K. Seo, S.J. Park, J. Mater. Sci. **37**, 1881 (2002)
51. B.J. Kim, K.M. Bae, M.K. Seo, K.H. An, S.J. Park, Mater. Sci. Eng., A **528**, 4953 (2011)
52. S.Y. Fu, B. Lauke, E. Mader, C.Y. Yue, X. Hu, Compos. Pt. A **31**, 1117 (2000)
53. S.J. Park, M.K. Seo, *Interface Science and Technology* (Elsevier, Nederland, 2011)
54. S.J. Park, Y.H. Chang, Y.C. Kim, K.Y. Rhee, J. Nanosci. Nanotechnol. **10**, 117 (2010)
55. M. Li, Y. Gu, Y. Liu, Y. Li, Z. Zhang, Carbon **52**, 1091 (2013)
56. L.Y. Yuan, S.S. Shyu, J.Y. Lai, J. Appl. Poly. Sci. **42**, 2525 (2003)
57. F. Mannocci, M. Sherriff, T.F. Watson, J. Endod. **27**, 758 (2001)
58. S.B. Kumar, S. Sivashanker, A. Bag, I. Sridhar, Mater. Sci. Eng., A **412**, 117 (2005)
59. S.U. Khan, A. Munir, R. Hussain, J.K. Kim, Compos. Sci. Technol. **70**, 2077 (2010)
60. I.S. Kim, Mater. Res. Bull. **33**, 1069 (1998)
61. S.J. Park, M.K. Seo, D.R. Lee, Carbon **41**, 2991 (2003)
62. F.A. Ramirez, L.A. Carlsson, B.A. Acha, Compos. Pt. A **40**, 679 (2009)
63. P. Compstona, P.Y.B. Jar, P.J. Burchill, K. Takahashi, Compos. Sci. Technol. **61**, 321 (2001)
64. G.R. Irwin, J.A. Kies, J. Welding **19**, 193 (1954)
65. L.A. Carlsson, J.W Gillespie, *Application of Fracture Mechanics to Composites* (Elsevier, Amsterdam, 1989)
66. S.J. Park, M.K. Seo, J.R. Lee, Compos. Interf. **13**, 249 (2006)
67. S. Kirdponpattara, M. Phisalaphong, B.Z. Newby, J. Colloid, Interface Sci. **397**, 169 (2013)
68. E.W. Washburn, Phys. Rev. **17**, 273 (1921)
69. D.K. Owens, R.C. Wendt, J. Appl. Polym. Sci. **13**, 1741 (1969)
70. D.H. Kaelble, J. Adhes. **2**, 66 (1970)
71. M.K. Seo, S.J. Park, J. Colloid Interface Sci. **330**, 237 (2009)
72. A. Hampe, G. Klinka, S. Meretz, E. Schulz, Composites **26**, 40 (1995)
73. E. Mader, K.H. Freitag, Composites **21**, 397 (1990)
74. W. Weibull, J. Appl. Mech. **18**, 293 (1951)
75. E.G. Stoner, *The Effect of Shape on the Tensile Strength of Pitch-based Carbon Fibers* (Clemson University, Clemson, SC, 1991)
76. S.J. Park, Y.S. Jang, J. Colloid Interface Sci. **237**, 91 (2001)
77. S.J. Park, M.K. Seo, H.Y. Kim, D.R. Lee, J. Colloid Interface Sci. **261**, 393 (2003)